國立臺灣大學工學院土木工程學系

碩士論文

Department of Civil Engineering
College of Engineering
National Taiwan University

Master Thesis

震動對邊坡顆粒流行為之研究:理論及實驗方法

Theoretical and experimental study of along-slope granular flow due to seismic shaking

葉欣宜

Hsin-Yi Yeh

指導教授：卡艾瑋 教授

Advisor: Dr. Hervé Capart

中華民國 105 年 7 月

July, 2016

doi:10.6342/NTU201603286

誌謝

doi:10.6342/NTU201603286

中文摘要

地震會影響邊坡的穩定性並導致邊坡滑落。本論文致力於探討地震對邊坡穩定性之影響，結合理論和實驗的方法以模擬在地震發生時，邊坡形貌的變化及顆粒流的運動模式。在理論部分，以質量、動量及動能守恆方程式為基礎，利用深度積分簡化顆粒流方程式，並驗證理論方法之可行性，再應用到模擬地震的方程式，將顆粒流方程式及深度積分方程式建立成數值計算模式，相互比較驗證，並進一步推導出加速度、通量和坡度之關係式。在實驗部分，利用振動台模擬地震波進行一系列實驗，將影像進行座標轉換及移除位移之校正後，再使用影像方法分析顆粒之流動形態，並觀察在振動情況下，物理量隨時間之變化。最後由實驗與理論之比較結果，發現在觀察通量及斜坡角度的關係時，實驗與理論模擬的結果有相似的趨勢，能夠幫助觀察及預測振動對邊坡之影響。

關鍵字：振動台實驗、顆粒流、邊坡滑動、粒子速度測量追蹤、深度積分

doi:10.6342/NTU201603286

ABSTRACT

Earthquakes can affect the stability of slope and trigger landslides. In this study, both theoretical and experimental analysis are used to comprehend the flows behavior of the slope under seismic conditions. Though theory, we develop a depth-integrated equations with the assumption of conservation of kinetic energy, mass and momentum. To solve the granular flow equations, we derive the numerical models from the local equations and the depth-integrated equations. A series of experiments is conducted on a shaking table, which can simulate the seismic vibration. We use the images from experiments and the particle tracking velocimetry (PTV) method to acquire the velocity fields, the depth of flow layer and the time-evolving variables. Using these approach, we develop a model that can be used to estimate the behavior of slope under seismic conditions. Through the theory and experiment results, we can know more about the mechanism of landslides once the shaking conditions are given.

Keywords： Seismic slope behavior; Granular flow; Shaking table model; Particle tracking velocimetry

doi:10.6342/NTU201603286

CONTENTS

doi:10.6342/NTU201603286

doi:10.6342/NTU201603286

LIST OF FIGURES

doi:10.6342/NTU201603286

doi:10.6342/NTU201603286

doi:10.6342/NTU201603286

doi:10.6342/NTU201603286

LIST OF TABLES

doi:10.6342/NTU201603286

Chapter 1 Introduction

In 1999, the Chi-Chi earthquake, also known as the 921 earthquake, struck Taiwan and triggered massive landslides, which caused a great deal of damage. Landslide is a natural phenomenon that occur when the slope is in an unstable condition. Earthquakes is one of the causes to trigger landslides. Due to the frequent earthquake, steep slope, and weak geological formation, there is a high probability that slope failures happened in Taiwan. In view of the risk, we would like to investigate this phenomenon.

Fig. 1-1 The earthquake-induced landslides during the Chi-Chi earthquake.

In the past, landslides triggered by earthquakes have been broadly discussed. We propose to focus on the slope behavior under seismic conditions in this research. In order to obtain more complete and reliable results, both theoretical and experimental analysis are used to simulate the motion. However, the seismic waves from earthquakes have a complex motion; therefore, the wave is simplified to a stable sine wave in our research.

Chou et al. (2013) conducted the experiments of dry granular piles with two

doi:10.6342/NTU201603286

symmetrical slopes under a horizontal shaking force. In the process, the relaxation of slope surface can be observed and the patterns on the granular surface are different under various shaking accelerations. In addition to the experiments, the equations to describe the process of relaxation are proposed in study. In our research, we design the experiment with one inclined granular slope and use the granular flow theory to describe the behavior of slope.

To analyze the slope behavior, we adopt the dense granular flow equations to model our case. For entraining granular flows in narrow channel, the depth-integrated equations can capture the flow process successfully (Capart et al. 2015). Therefore, we apply the depth-integrated equation to solve our problem. In order to check these two methods both can obtain the velocity field and flow layer of the slope, we compare the calculation results together to verify the applicability. Furthermore, we find the relation between slope and acceleration by the results of depth-integrated equation. This equation can provide the estimation of equilibrium angle.

The laboratory experiments are conducted on a shaking table, which can simulate the seismic vibration. We use the glossy mill stones as material to build the model slope, and take several measurements under different acceleration condition. After that, the image method is used to analyze the measurements. With the experimental results, we can convert them into the data which we are interest in, and compare them with the theoretical results.

doi:10.6342/NTU201603286

Chapter 2 Theory

In this research, we employ the theory of granular flow over loose bed to describe the behavior of granular flow due to seismic shaking. Before discussing the influence of seismic, we consider the basic problem first. Besides the local equations, we apply the depth-integrated equations to study the behavior. Then, we compare the results of two kinds of equations with the analytic solution to check the applicability of these approaches. After that, we can apply these methods to our case to obtain the results. Moreover, we derive the semi-analytical solution to find the relation of slope and acceleration and the relation of slope and flux by applying the depth-integrated equations.

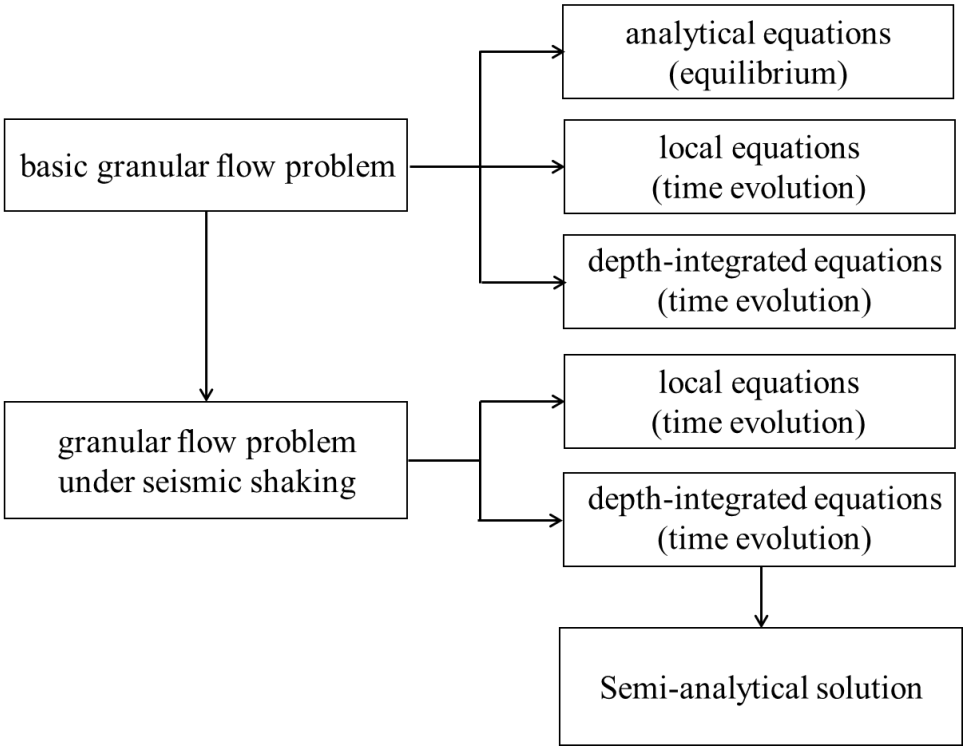

Fig. 2-1 Procedure of theory analysis

doi:10.6342/NTU201603286

2.1 Unsteady uniform granular flows over erodible bed

2.1.1 Local equations

In the case of a dense granular flow over loose bed in a narrow channel, we apply the theory of granular flows in channels (Capart et al. 2015) to the basic problem. The governing equations can be obtained according to the mass and momentum balances.

$$\begin{cases} \dfrac{\partial u}{\partial x}+\dfrac{\partial w}{\partial z}=0 \\ \rho\dfrac{\partial u}{\partial t}=\rho g\sin\beta+\dfrac{\partial \tau}{\partial z}-2\dfrac{\tau_W}{W} \\ \dfrac{\partial \sigma}{\partial z}=-\rho g\cos\beta \end{cases} \tag{2.1}$$

where x and z are the coordinates parallel and perpendicular to the flow direction, t is time, u and w are the velocity components in x and z direction, W is the width of channel, α is the angle of repose, β is the inclination of channel, the bulk density is $\rho=c_s\rho_s$, the shear stress act on the wall is $\tau_W=\mu_W\sigma$, the normal stress is $\sigma=\rho g_\perp\left(\tilde{z}-z\right)$. We define the components of gravitational acceleration are $g_\parallel=g\sin\alpha$ and $g_\perp=g\cos\alpha$. As for the internal shear stress, we adopt the linearized dense granular flow rheology (GDR MiDi 2004; da Cruz et al. 2005; Berzi and Jenkins 2009)

$$\tau=\left(\tan\alpha+\chi I\right)\sigma \quad , \quad \mathrm{I}=\frac{\dot{\gamma}D}{\sqrt{\sigma/(\mathrm{c}_s\,\rho_s)}} \tag{2.2}$$

$$\tau=\tan\alpha\sigma+\chi D\sqrt{\rho\sigma}\dot{\gamma} \tag{2.3}$$

where χ is the dimensionless rheological coefficient, $\dot{\gamma}=\dfrac{\partial u}{\partial z}$ is shear rate, D is the grain diameter. The variables are defined in Fig. 2-2.

doi:10.6342/NTU201603286

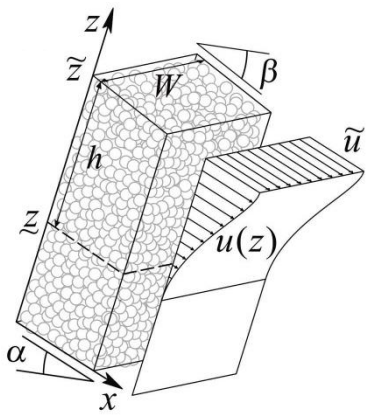

Fig. 2-2 Variable definitions of a dense granular flow over loose bed in a narrow channel (Hung, 2015)

The boundary conditions is

$$\tilde{\tau} = 0, \quad \tilde{\sigma}=0, \quad \underline{z} > 0, \quad \underline{u}=0, \quad \underline{\tau} = \tan\alpha\,\underline{\sigma} \tag{2.4}$$

At equilibrium, the depth, depth-averaged velocity, and velocity profile are

$$h = (\tan\beta - \tan\alpha)\frac{W}{\mu_W} \tag{2.5}$$

$$\bar{u} = \frac{4}{35}\frac{g_\perp^{1/2}}{\chi D}\left(\tan\beta - \tan\alpha\right)^{5/2}\left(\frac{W}{\mu_W}\right)^{3/2} \tag{2.6}$$

$$u = \bar{u} f\left(\hat{\eta}\right) \tag{2.7}$$

$$\hat{\eta} = \left(\tilde{z} - z\right)/h \quad , \quad f\left(\hat{\eta}\right) = \frac{7}{3} - \frac{35}{6}\hat{\eta}^{3/2} + \frac{7}{2}\hat{\eta}^{5/2} \tag{2.8}$$

where η is the depth coordinate measured from free surface. In addition, we are also interested in the non-equilibrium evolution. Thus, we solve the equations by using explicit finite difference scheme, and rewrite (2.1) into the recurrence equation.

$$\frac{u_i^{(t+1)} - u_i^{(t)}}{\Delta t} = g_{\parallel} - \frac{1}{\rho}\frac{\tau_{i+\frac{1}{2}} - \tau_{i-\frac{1}{2}}}{\Delta\eta} - 2\frac{\tau_{W,i}}{W} \tag{2.9}$$

doi:10.6342/NTU201603286

where

$$\tau_{i+\frac{1}{2}} = \tan\alpha\sigma_{i+\frac{1}{2}} - \chi D\sqrt{\rho\sigma_{i+\frac{1}{2}}}\frac{u_{i+1}^{(t)} - u_i}{\Delta\eta} \quad (2.10)$$

$$\tau_{i-\frac{1}{2}} = \tan\alpha\sigma_{i-\frac{1}{2}} - \chi D\sqrt{\rho\sigma_{i-\frac{1}{2}}}\frac{u_i^{(t)} - u_{i-1}^{(t)}}{\Delta\eta} \quad (2.11)$$

$$\tau_{W,i} = \mu_W\sigma_i = \mu_W\rho g_\perp\eta_i \quad (2.12)$$

2.1.2 Depth-integrated equations

To get the non-equilibrium evolution by another method, we adopt the depth-integrated equations, which proposed by Capart *et al*. (2015), to solve the same governing equations. We assume that the velocity profile remains self-similar

$$u(z,t) = \bar{u}(t)f(\hat{z}) \quad (2.13)$$

Integrate the momentum equation over depth,

$$\int_0^{h(t)}\frac{\partial u}{\partial t}d\eta = \int_0^{h(t)}\left(g_\parallel + \frac{1}{\rho}\frac{\partial\tau}{\partial z} - 2\frac{\tau_W}{\rho W}\right)d\eta \quad (2.14)$$

Calculate term by term

$$\int_0^{h(t)}\frac{\partial u}{\partial t}d\eta = \frac{\partial}{\partial t}\int_0^{h(t)}u(\eta,t)d\eta = \frac{\partial}{\partial t}(h\bar{u}) \quad (2.15)$$

$$\int_0^{h(t)}\frac{1}{\rho}\frac{\partial\tau}{\partial z}d\eta = -\tan\alpha g_\perp h \quad (2.16)$$

$$\int_0^{h(t)}2\frac{\tau_W}{\rho W}d\eta = \frac{\mu_W}{W}g_\perp h^2 \quad (2.17)$$

Thus, we get the ordinary differential equation for the depth-integrated momentum

$$\frac{d}{dt}(h\bar{u}) = g_\perp(\tan\beta - \tan\alpha)h - \frac{\mu_W}{W}g_\perp h^2 \quad (2.18)$$

Since there are two variables to determine, we need another equation to solve the problem. Hence we integrate the equation over depth again and weight by the local velocity $u(z)$,

doi:10.6342/NTU201603286

$$\int_0^{h(t)} u\frac{\partial u}{\partial t}d\eta = \int_0^{h(t)} u\left(g_{\parallel} + \frac{1}{\rho}\frac{\partial \tau}{\partial z} - 2\frac{\tau_W}{\rho W}\right)d\eta \qquad (2.19)$$

and get another ordinary differential equation for the depth-integrated kinetic energy

$$\frac{d}{dt}\left(\frac{77}{96}h\bar{u}^2\right) = g_{\perp}(\tan\beta - \tan\alpha)h\bar{u} - \frac{35}{9}\chi D\sqrt{g_{\perp}h}\frac{\bar{u}^2}{h} - \frac{5}{9}\frac{\mu_W}{W}g_{\perp}h^2\bar{u} \qquad (2.20)$$

In order to solve the ordinary differential equations, we rewrite these two equations into separate ordinary differential equations of $\bar{u}(t)$ and $h(t)$

$$\frac{d\bar{u}}{dt} = \frac{19}{77}g_{\perp}(\tan\beta - \tan\alpha) - \frac{160}{33}\chi D\sqrt{g_{\perp}}\frac{\bar{u}}{h^{\frac{3}{2}}} + \frac{71}{231}\frac{\mu_W}{W}g_{\perp}h \qquad (2.21)$$

$$\frac{dh}{dt} = \frac{58}{77}g_{\perp}(\tan\beta - \tan\alpha)\frac{h}{\bar{u}} + \frac{160}{33}\chi D\sqrt{g_{\perp}}\frac{1}{h^{\frac{1}{2}}} - \frac{302}{231}\frac{\mu_W}{W}g_{\perp}\frac{h^2}{\bar{u}} \qquad (2.22)$$

2.1.3 Comparison

In order to check the results of these two methods, we solve the governing equations and depth-integrated equations to get the non-equilibrium evolution, and compare with the analytical solution. The results are plotted together in Fig. 2-3, and we can find the profiles are congruent. It means that both of these two methods enable us to solve the problem. The numerical scheme used is presented in section 2.2.3.

doi:10.6342/NTU201603286

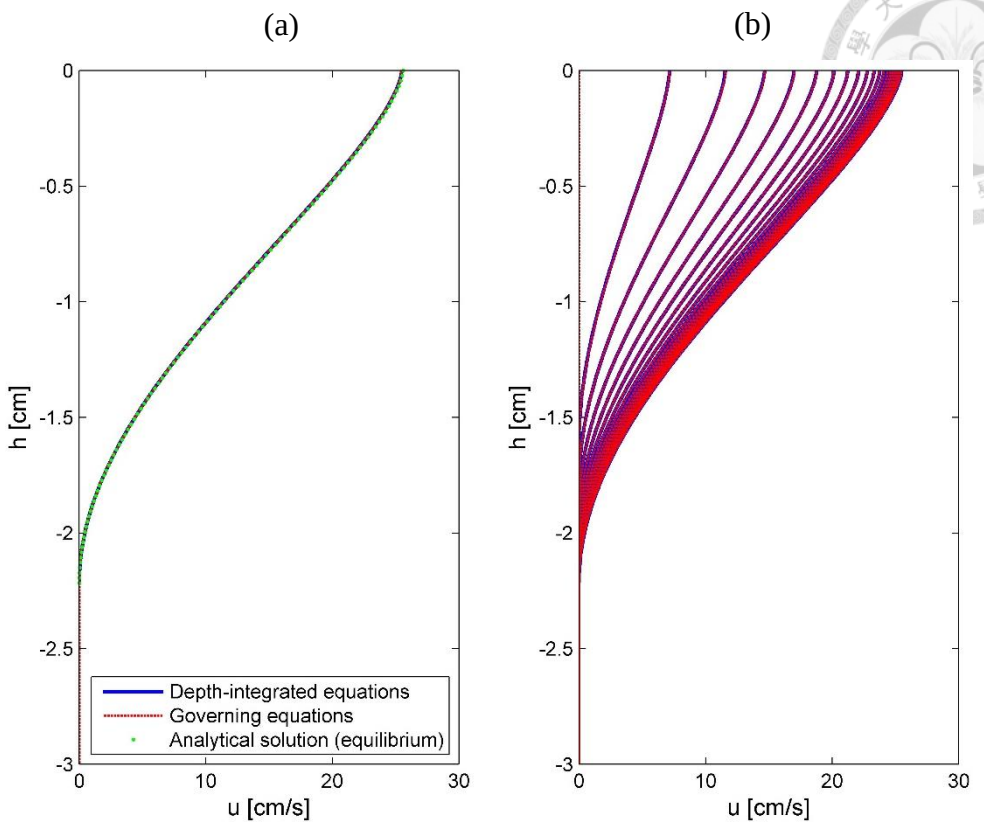

Fig. 2-3 Velocity profile: (a) Equilibrium (b) Evolution

2.2 Unsteady uniform granular flows due to seismic shaking

2.2.1 Local equations

After the approach is verified, we apply the granular flow rheology to our case. First, the acceleration term needs to be revised, so we assume the direction of vibration acceleration is parallel to the ground and the acceleration changes periodically which is defined as $a\sin\omega t$. Moreover, the surface is parallel to the inclination β of the rigid bottom of the channel. Thus, the parallel and perpendicular components of acceleration can be defined as $g\sin\beta + a\sin\omega t\cos\beta$ and $g\cos\beta - a\sin\omega t\sin\beta$ as shown in Fig. 2-4. In our case, the governing equation is

doi:10.6342/NTU201603286

$$\begin{cases} \rho\dfrac{\partial u}{\partial t} = \rho\left(g\sin\beta + a\cos\beta\sin\omega t\right) + \dfrac{\partial\tau}{\partial z} - 2\dfrac{\tau_W}{W} \\ \dfrac{\partial\sigma}{\partial z} = -\rho\left(g\cos\beta - a\sin\beta\sin\omega t\right) \end{cases} \tag{2.23}$$

where the shear stress is $\tau = \tan\alpha\sigma + \chi D\sqrt{\rho\sigma}\dot{\gamma}$, $\tau_W = \mu_W\sigma$, and the boundary conditions is $\tilde{\tau} = 0$, $\tilde{\sigma}$=0, $\underline{z} > 0$, $\underline{u}$=0, $\underline{\tau} = \tan\alpha\underline{\sigma}$.

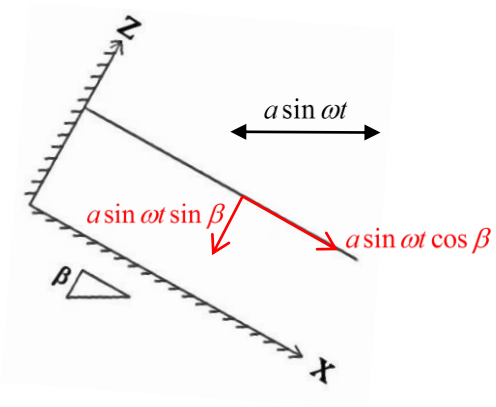

Fig. 2-4 the components of vibration acceleration: parallel ($a\sin\omega t\cos\beta$) and perpendicular ($a\sin\omega t\sin\beta$) to the flow direction

The direction of flow velocity will change in our case, because the channel moves back and forth periodically. Theoretically, the shear stress resists the motion of particles, so the direction of friction terms are opposite to the direction of velocity. Therefore, it is necessary to define the direction of friction terms in particular when we solve the equations by numerical method. We use (2.24) to revise the velocity terms.

$$\frac{\partial u}{\partial z} = \frac{\dfrac{\partial u}{\partial z}}{\left|\dfrac{\partial u}{\partial z}\right|}\cdot\frac{\partial u}{\partial z} \tag{2.24}$$

doi:10.6342/NTU201603286

The internal shear stress is revised to

$$\tau = \frac{\partial u}{\partial z}\left(\frac{\tan\alpha\sigma}{\left|\frac{\partial u}{\partial z}\right|} + \chi D\sqrt{\rho\sigma} \right) \tag{2.25}$$

$$\tau_{i+\frac{1}{2}} = \frac{u_{i+1}-u_i}{\Delta z}\cdot\rho\left[\frac{\tan\alpha g_\perp\left(\tilde{z}-z_{i+\frac{1}{2}}\right)}{\left|\frac{u_{i+1}-u_i}{\Delta z}\right|} + \chi D\sqrt{g_\perp\left(\tilde{z}-z_{i+\frac{1}{2}}\right)} \right] = \frac{u_{i+1}-u_i}{\Delta z}\cdot\rho\cdot\nu_{i+\frac{1}{2}}$$

$$\tau_{i-\frac{1}{2}} = \frac{u_i-u_{i-1}}{\Delta z}\cdot\rho\left[\frac{\tan\alpha g_\perp\left(\tilde{z}-z_{i-\frac{1}{2}}\right)}{\left|\frac{u_i-u_{i-1}}{\Delta z}\right|} + \chi D\sqrt{g_\perp\left(\tilde{z}-z_{i-\frac{1}{2}}\right)} \right] = \frac{u_i-u_{i-1}}{\Delta z}\cdot\rho\cdot\nu_{i-\frac{1}{2}}$$

$$\frac{\partial\tau}{\partial z} = \frac{\tau_{i+\frac{1}{2}}-\tau_{i-\frac{1}{2}}}{\Delta z} = \rho\left[\frac{\nu_{i+\frac{1}{2}}}{\Delta z^2}u_{i+1} - \left(\frac{\nu_{i+\frac{1}{2}}}{\Delta z^2}+\frac{\nu_{i-\frac{1}{2}}}{\Delta z^2}\right)u_i + \frac{\nu_{i-\frac{1}{2}}}{\Delta z^2}u_{i-1} \right]$$

The shear stress act on the wall is

$$\tau_W = \mu_W\sigma = \mu_W g_\perp\left(\tilde{z}-z_i\right)\frac{u_i}{|u_i|} \tag{2.26}$$

We can rewrite (2.23) into the recurrence equation.

$$\frac{u_i^{t+\Delta t}-u_i^t}{\Delta t} = (g\sin\beta + a\cos\beta\sin\omega t) + \left[\frac{\nu_{i+\frac{1}{2}}}{\Delta z^2}u_{i+1}^{t+\Delta t} - \left(\frac{\nu_{i+\frac{1}{2}}}{\Delta z^2}+\frac{\nu_{i-\frac{1}{2}}}{\Delta z^2}\right)u_i^{t+\Delta t} + \frac{\nu_{i-\frac{1}{2}}}{\Delta z^2}u_{i-1}^{t+\Delta t} \right] \tag{2.27}$$
$$-2\frac{\mu_W}{\rho W}g_\perp\left(\tilde{z}-z_i\right)\frac{u_i^{t+\Delta t}}{\left|u_i^{t+\Delta t}\right|}$$

doi:10.6342/NTU201603286

2.2.2 Depth-integrated equations

As mentioned previously, the depth-integrated equations also can be used to solve the governing equation. We can obtain the depth-integrated momentum equation and the depth-integrated kinetic energy equation by integrate the governing equation over depth. To revise the velocity terms, we add the sign function $\mathrm{sgn}(\bar{u})$ to equations.

$$\begin{aligned}\frac{d}{dt}\left(h\bar{u}\right) &= (g_{\parallel} + a\cos\beta\sin\omega t)h - \tan\alpha\left(g_{\perp} - a\sin\beta\sin\omega t\right)h\cdot\mathrm{sgn}(\bar{u}) \\ &\quad -\frac{\mu_W}{W}\left(g_{\perp} - a\sin\beta\sin\omega t\right)h^2\cdot\mathrm{sgn}(\bar{u})\end{aligned} \tag{2.28}$$

$$\begin{aligned}\frac{d}{dt}\left(\frac{77}{96}h\bar{u}^2\right) &= (g_{\parallel} + a\cos\beta\sin\omega t)h\bar{u} - \tan\alpha\left(g_{\perp} - a\sin\beta\sin\omega t\right)h\bar{u}\cdot\mathrm{sgn}(\bar{u}) \\ &\quad -\frac{35}{9}\chi D\sqrt{\left(g_{\perp} - a\sin\beta\sin\omega t\right)h}\,\frac{\bar{u}^2}{h} \\ &\quad -\frac{5}{9}\frac{\mu_W}{W}\left(g_{\perp} - a\sin\beta\sin\omega t\right)h^2\bar{u}\cdot\mathrm{sgn}(\bar{u})\end{aligned} \tag{2.29}$$

The equations can separate into two ordinary differential equations of $\bar{u}(t)$ and $h(t)$

$$\begin{aligned}\frac{d\bar{u}}{dt} &= \frac{19}{77}\left[g_{\parallel} + a\cos\beta\sin\omega t - \tan\alpha\cdot(g_{\perp} - a\sin\beta\sin\omega t)\cdot\mathrm{sgn}(\bar{u})\right] \\ &\quad -\frac{160}{33}\chi D\sqrt{(g_{\perp} - a\sin\beta\sin\omega t)}\,\frac{\bar{u}}{h^{\frac{3}{2}}} + \frac{71}{231}\frac{\mu_W}{W}(g_{\perp} - a\sin\beta\sin\omega t)h\cdot\mathrm{sgn}(\bar{u})\end{aligned} \tag{2.30}$$

$$\begin{aligned}\frac{dh}{dt} &= \frac{58}{77}\left[g_{\parallel} + a\cos\beta\sin\omega t - \tan\alpha\cdot(g_{\perp} - a\sin\beta\sin\omega t)\cdot\mathrm{sgn}(\bar{u})\right]\frac{h}{\bar{u}} \\ &\quad +\frac{160}{33}\chi D\sqrt{(g_{\perp} - a\sin\beta\sin\omega t)}\,\frac{1}{h^{\frac{1}{2}}} - \frac{302}{231}\frac{\mu_W}{W}(g_{\perp} - a\sin\beta\sin\omega t)\frac{h^2}{\bar{u}}\cdot\mathrm{sgn}(\bar{u})\end{aligned} \tag{2.31}$$

doi:10.6342/NTU201603286

2.2.3 Numerical scheme and comparison

The two ordinary differential equations of $\bar{u}(t)$ and $h(t)$ derived from the depth-integrated equations can rewrite into the recurrence equation.

$$\frac{d\bar{u}}{dt}=\frac{\bar{u}^{(k+1)}-\bar{u}^{(k)}}{\Delta t}=A(t)-\mathrm{B}(t)\cdot\frac{\bar{u}^{(k+1)}}{\left|\bar{u}^{(k)}\right|+\lambda_{\bar{u}}}+C(t)\cdot\frac{\bar{u}^{(k+1)}}{\left|\bar{u}^{(k)}\right|+\lambda_{\bar{u}}}\cdot h^{(k)}-\mathrm{J}(t)\frac{\bar{u}^{(k)}}{\left(h^{(k)}+\lambda_h\right)^{\frac{3}{2}}} \tag{2.32}$$

$$\frac{dh}{dt}=\frac{h^{(k+1)}-h^{(k)}}{\Delta t}=E(t)\frac{h^{(k+1)}\cdot\bar{u}^{(k+1)}}{\left(\left|\bar{u}^{(k)}\right|+\lambda_{\bar{u}}\right)^2}-F(t)\frac{h^{(k+1)}}{\left|\bar{u}^{(k)}\right|+\lambda_{\bar{u}}}-G(t)\frac{\left(h^{(k+1)}\right)^2}{\left|\bar{u}^{(k)}\right|+\lambda_{\bar{u}}}+I(t)\frac{1}{\left(h^{(k)}+\lambda_h\right)^{\frac{1}{2}}} \tag{2.33}$$

where $A(t)=\frac{19}{77}\left(g_{\parallel}+a\cos\beta\sin\omega t\right)$, $B(t)=\frac{19}{77}\tan\alpha(g_{\perp}-a\sin\beta\sin\omega t)$,

$$C(t)=\frac{71}{231}\frac{\mu_W}{W}(g_{\perp}-a\sin\beta\sin\omega t),\ \mathrm{J}(t)=\frac{160}{33}\chi D\sqrt{(g_{\perp}-a\sin\beta\sin\omega t)},$$

$$E(t)=\frac{58}{77}\left(g_{\parallel}+a\cos\beta\sin\omega t\right),\ F(t)=\frac{58}{77}\tan\alpha(g_{\perp}-a\sin\beta\sin\omega t),$$

$$G(t)=\frac{302}{231}\frac{\mu_W}{W}(g_{\perp}-a\sin\beta\sin\omega t),\ I(t)=\frac{160}{33}\chi D\sqrt{(g_{\perp}-a\sin\beta\sin\omega t)}$$

Then, we transpose the equation, and we can obtain the depth-averaged velocity and flow depth from (2.34) and (2.35).

$$\bar{u}^{(k+1)}=\frac{\left[1-\frac{\mathrm{J}(t)\cdot\Delta t}{\left(h^{(k)}+\lambda_h\right)^{\frac{3}{2}}}\right]\bar{u}^{(k)}+A(t)\Delta t}{1+\frac{\mathrm{B}(t)\cdot\Delta t}{\left|\bar{u}^{(k)}\right|+\lambda_{\bar{u}}}-\frac{C(t)\cdot\Delta t\cdot h^{(k)}}{\left|\bar{u}^{(k)}\right|+\lambda_{\bar{u}}}} \tag{2.34}$$

doi:10.6342/NTU201603286

$$\frac{G(t)\cdot\Delta t}{\left|\bar{u}^{(k)}\right|+\lambda_{\bar{u}}}\left(h^{(k+1)}\right)^2+\left[1+\frac{F(t)\Delta t}{\left|\bar{u}^{(k)}\right|+\lambda_{\bar{u}}}-\frac{E(t)\Delta t\cdot\bar{u}^{(k+1)}}{\left(\left|\bar{u}^{(k)}\right|+\lambda_{\bar{u}}\right)^2}\right]h^{(k+1)}=h^{(k)}+\frac{I(t)\Delta t}{\left(h^{(k)}+\lambda_h\right)^{\frac{1}{2}}} \quad (2.35)$$

The results of the depth-integrated equations are compared with the local solutions solved by Capart (2016). We consider the one way flow and the two way flow. The numerical parameters are listed in Table 2.1. The results are plotted from

Fig. 2-5 to Fig. 2-8. We can observe that the results obtained by the local equations and the depth-integrated equations are similar. It means that these two methods are available to solve our seismic shaking problem.

Table 2.1 Numerical parameters

Parameter	Symbol	One way flow Value [Unit]	Two way flow Value [Unit]
Gravity acceleration	g	$9.8\left[m/s^2\right]$	$9.8\left[m/s^2\right]$
Angle of repose	$\tan\alpha$	0.3	0.3
Inclination of the channel	$\tan\beta$	0.15	0.05
Horizontal shaking acceleration	a	$0.3g\left[m/s^2\right]$	$0.5g\left[m/s^2\right]$
Frequency	f	$4\left[Hz\right]$	$4\left[Hz\right]$
Rheological parameter	χ	0.5	0.5
Grain diameter	D	$0.0023\left[m\right]$	$0.0023\left[m\right]$
Wall friction coefficient	μ_W	0.2	0.2
Width of channel	W	$0.04\left[m\right]$	$0.04\left[m\right]$
Minimum value	$\lambda_{\bar{u}}$	10^{-6}	10^{-6}
Minimum value	λ_h	10^{-6}	10^{-6}
Time interval	Δt	$10^{-5}\left[s\right]$	$10^{-5}\left[s\right]$

doi:10.6342/NTU201603286

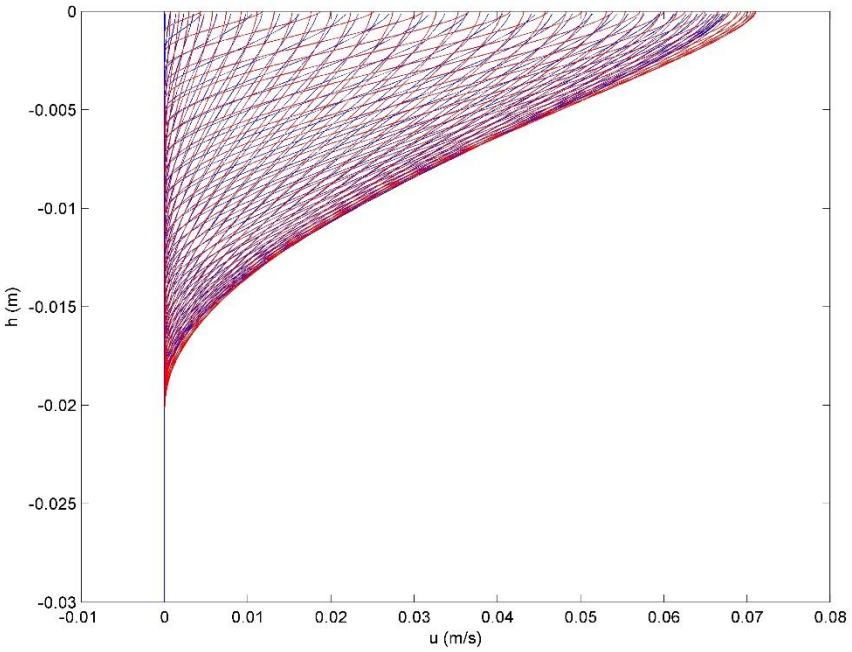

Fig. 2-5 the velocity profile of one way flow: The blue lines are local solutions, the red lines are the results of the depth-integrated equations.

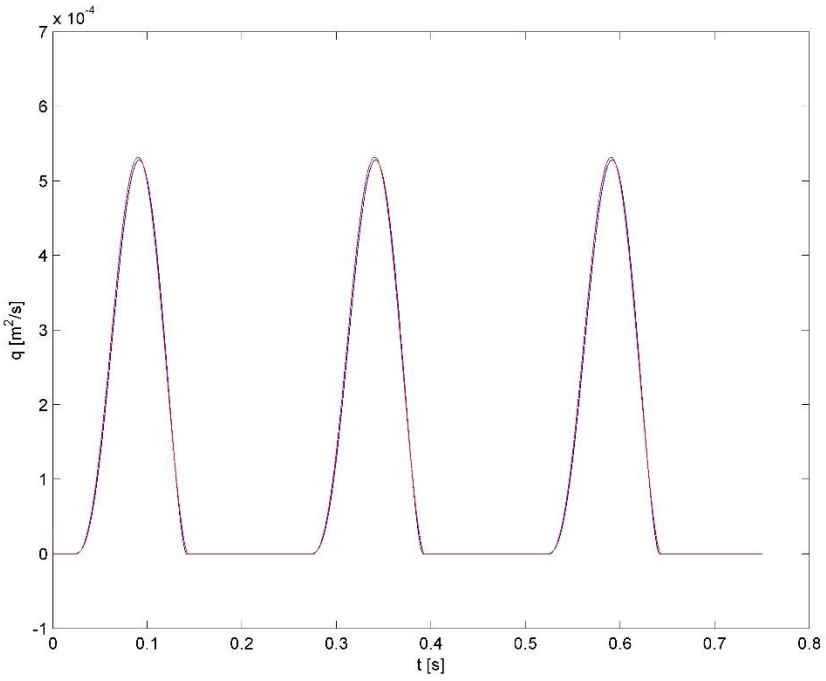

Fig. 2-6 the flux of one way flow: The blue lines are local solutions, the red lines are the results of the depth-integrated equations.

doi:10.6342/NTU201603286

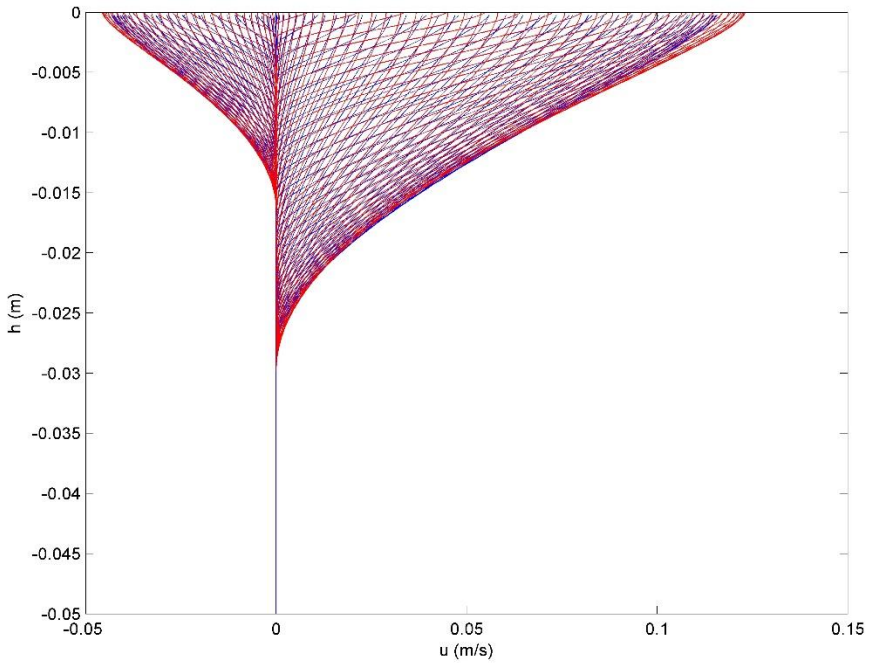

Fig. 2-7 the velocity profile of two way flow: The blue lines are local solutions, the red lines are the results of the depth-integrated equations.

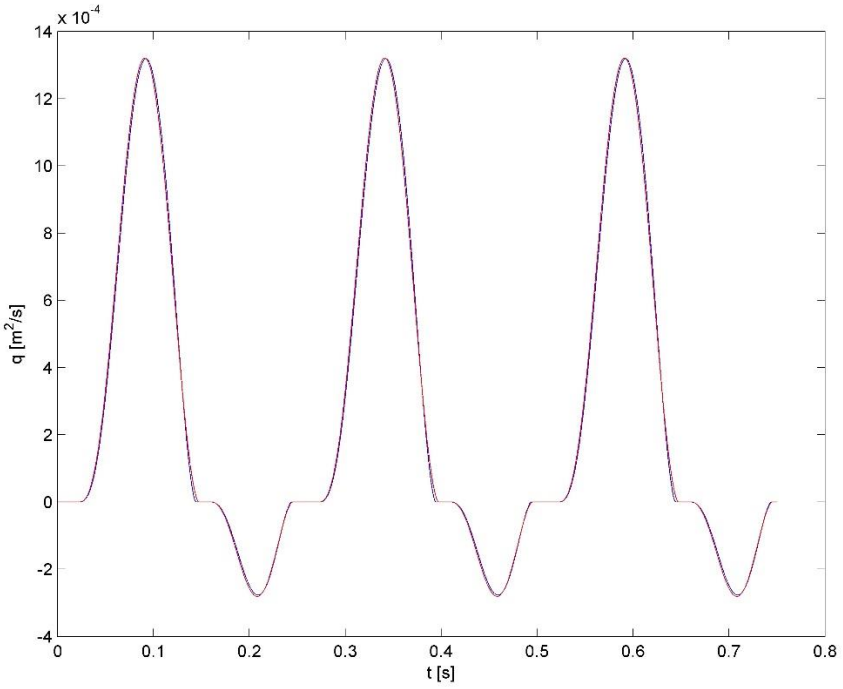

Fig. 2-8 the flux of two way flow: The blue lines are local solutions, the red lines are the results of the depth-integrated equations.

doi:10.6342/NTU201603286

2.3 Semi-analytical solution

2.3.1 The relation between slope and acceleration

We can employ the equations (2.30) and (2.31) to find the condition of critical state. Consider that there is no flow under critical state, the term to decide the flow state is

$$f(t) = g_{\parallel} + a\cos\beta\sin\omega t - \tan\alpha\cdot(g_{\perp} - a\sin\beta\sin\omega t)\cdot\mathrm{sgn}(\bar{u}) \tag{2.36}$$

and when $\sin\omega t = 1$, the $f(t)$ achieve the maximum value

$$f_{\max} = g_{\parallel} + a\cos\beta - \tan\alpha\cdot(g_{\perp} - a\sin\beta) \tag{2.37}$$

If $f_{\max} = 0$, the flow is in the critical state. Thus, we can obtain the relation between slope and acceleration in critical state.

$$f_{\max} = g_{\parallel} + a\cos\beta_c - \tan\alpha\cdot(g_{\perp} - a\sin\beta_c) = 0$$

and transpose the equation

$$\tan\beta_c = \frac{\tan\alpha\cdot g - a}{\tan\alpha\cdot a + g} \tag{2.38}$$

2.3.2 The relation between slope and flux

As mentioned previously, the parallel and perpendicular components of acceleration are defined as

$$g_{\parallel}(t) \triangleq g\sin\beta + a\cos\beta\sin\omega t \tag{2.39}$$

$$g_{\perp}(t) \triangleq g\cos\beta - a\sin\beta\sin\omega t \tag{2.40}$$

We try to simplify the equations to find a semi-analytical solution of the relation between slope and flux. With the equation (2.37), the condition to let $f(t)$ be maximum is

$$\omega t \approx \frac{\pi}{2} \tag{2.41}$$

doi:10.6342/NTU201603286

We assume $x = \omega t - \frac{\pi}{2}$ and use a Taylor series for $\sin \omega t$ at $\omega t = \frac{\pi}{2} + x \ \left(x \approx 0 \right)$

$$\sin \omega t = \sin\left(\frac{\pi}{2} + x \right) \approx \sin\left(\frac{\pi}{2} \right) + \cos\left(\frac{\pi}{2} \right) x - \sin\left(\frac{\pi}{2} \right) \frac{x^2}{2} \tag{2.42}$$

$$\sin \omega t \approx 1 - \frac{1}{2}\left(\omega t - \frac{\pi}{2} \right)^2 \tag{2.43}$$

According to the result of Taylor series expansions for $\sin \omega t$, we simplify the sinusoidal wave to a parabola. Then, we redefine the parallel and perpendicular components of acceleration with (2.43). Since the value of shaking acceleration and inclination influence the sign of parallel components of acceleration, we still need to consider the effect of time term. Thus, the simplified parallel components of acceleration is

$$g_{\parallel}\left(t \right) \approx g \sin \beta + a \cos \beta \left[1 - \frac{1}{2}\left(\omega t - \frac{\pi}{2} \right)^2 \right] \tag{2.44}$$

As for the perpendicular components of acceleration, we can simplify as

$$g_{\perp} \approx g \cos \beta - a \sin \beta \tag{2.45}$$

With the simplified definitions of acceleration, the equation (2.36) can be written as

$$f\left(t \right) = g \sin \beta + a \cos \beta \left[1 - \frac{1}{2}\left(\omega t - \frac{\pi}{2} \right)^2 \right] - \tan \alpha \left(g \cos \beta - a \sin \beta \right) \tag{2.46}$$

The flow starts to have velocity when $f\left(t \right)$ is zero. We assume the time that the flow starts to have velocity is t_0, and the time that the flow back to static is t_1.

$$f\left(t_0 \right) = g \sin \beta + a \cos \beta \left[1 - \frac{1}{2}\left(\omega t_0 - \frac{\pi}{2} \right)^2 \right] - \tan \alpha \left(g \cos \beta - a \sin \beta \right) = 0$$

$$t_0 = \frac{1}{\omega}\left(\frac{\pi}{2} - \sqrt{2 \frac{f_{\max}}{a \cos \beta}} \right) \tag{2.47}$$

As shown in Fig. 2-9, we can observe that $f\left(t \right)$ is similar within the time period from

doi:10.6342/NTU201603286

t_0 to t_1. It means that our simplification is available.

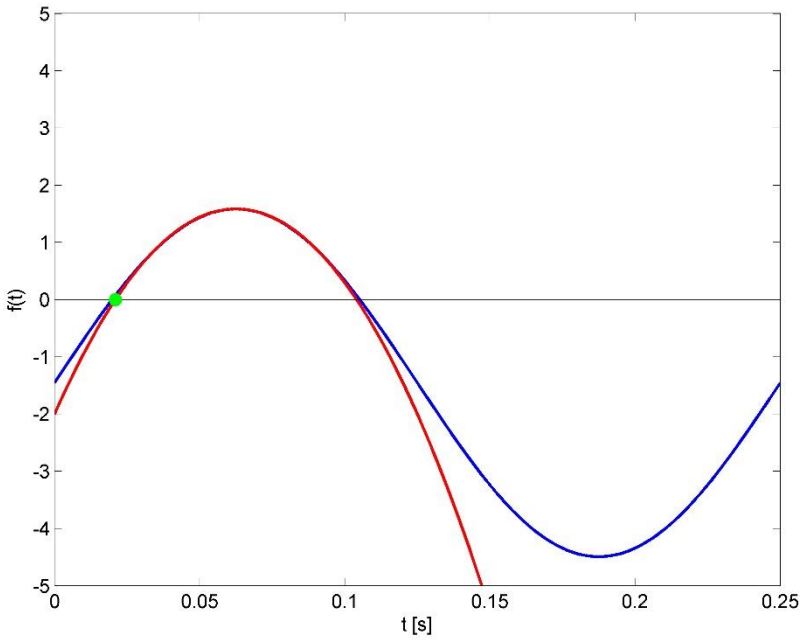

Fig. 2-9 The simplification of $f(t)$: The blue line is sinusoidal wave, the red line is a parabola, and the green point is at $t = t_0$.

We simplify the equation (2.30) and (2.31),

$$\frac{d\bar{u}}{dt} = \frac{19}{77} f(t) + \frac{71}{231} \frac{\mu_W}{W} g_\perp h \tag{2.48}$$

$$\frac{dh}{dt} = \frac{58}{77} f(t) \frac{h}{\bar{u}} - \frac{302}{231} \frac{\mu_W}{W} g_\perp \frac{h^2}{\bar{u}} \tag{2.49}$$

Then, we define the dimensionless variables $\hat{f}(\hat{t})$, $\hat{t}$, $\hat{\bar{u}}$, $\hat{h}$, and the equation (2.48) and (2.49) become

$$\frac{d\hat{\bar{u}}}{d\hat{t}} = \frac{19}{77} \hat{f}(\hat{t}) + \frac{71}{231} \hat{h} \tag{2.50}$$

$$\frac{d\hat{h}}{d\hat{t}} = \frac{58}{77} \hat{f}(\hat{t}) \frac{\hat{h}}{\hat{\bar{u}}} - \frac{302}{231} \frac{\hat{h}^2}{\hat{\bar{u}}} \tag{2.51}$$

doi:10.6342/NTU201603286

where $\hat{f}(\hat{t}) = \frac{f(t)}{f_{max}}$, $\hat{t} = \frac{t}{t_{max}}$, $\hat{\bar{u}} = \frac{\bar{u}}{f_{max} \cdot t_{max}}$, $\hat{h} = \frac{\mu_W \cdot g_\perp}{f_{max} \cdot W} h$

As the results of dimensionless equations, we know that

$$q \propto \frac{{f_{max}}^3 \cdot W / \mu_W}{a \cos\beta \cdot \omega \cdot g_\perp} \tag{2.52}$$

We substitute the parameters into (2.52) to find the coefficient

$$q = C \cdot \frac{{f_{max}}^3 \cdot W / \mu_W}{a \cos\beta \cdot \omega \cdot g_\perp} \tag{2.53}$$

$$C = \frac{q}{\frac{{f_{max}}^3 \cdot W / \mu_W}{a \cos\beta \cdot \omega \cdot g_\perp}} = \frac{\frac{\int_{t_0}^{t_1} q dt}{T}}{\frac{{f_{max}}^3 \cdot W / \mu_W}{a \cos\beta \cdot \omega \cdot g_\perp}} = 0.1175 \tag{2.54}$$

doi:10.6342/NTU201603286

Chapter 3 Shaking table experiment

In this chapter, we will introduce the setup, facilities and procedures of our experiments at first. Since the image method is used to analyze the experimental results, we need to adjust the photos, and the method and process will be discussed later. Finally, we will check the repeatability of experiments.

3.1 Experimental setup

The experimental apparatus is composed of the channel, the shaking table, cameras, particles, and other auxiliary equipment (Fig. 3-1). We will introduce each device and discuss the experimental design in this section.

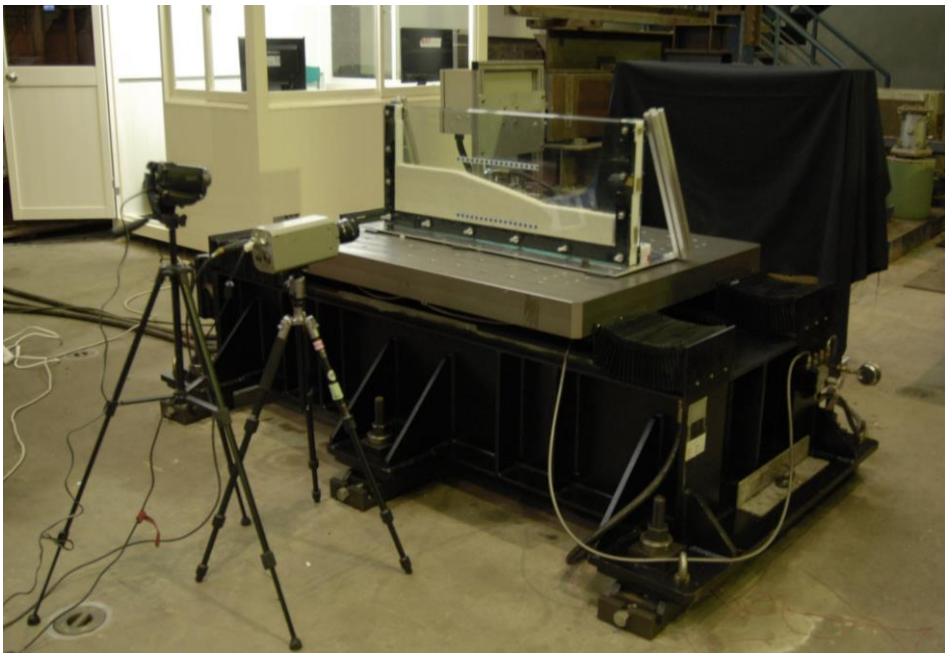

Fig. 3-1 Overview of the experimental apparatus

The design of the channel is illustrated in Fig. 3-2 with a length of 100 cm, width of 4 cm, and height of 40 cm. Since particles will rub against the walls of the channel, we use glass as the material of channel to reduce quantity of scratches caused by particles inside the channel. Moreover, glass is not easily bent or deformed after conducting

doi:10.6342/NTU201603286

experiments. Then, polyethylene blocks are placed between two sheets of glass and be screwed together. We can alter the width of channel with different block sizes. Since the polyethylene blocks are removable, the object can be easily cleared from the channel. In addition, we put an aluminum sheet under the channel in order to fix the channel to the shaking table. One side of the channel is connected to the aluminum sheet, the other side can be adjusted to our design width of channel. The overall view of the channel is shown in Fig. 3-3.

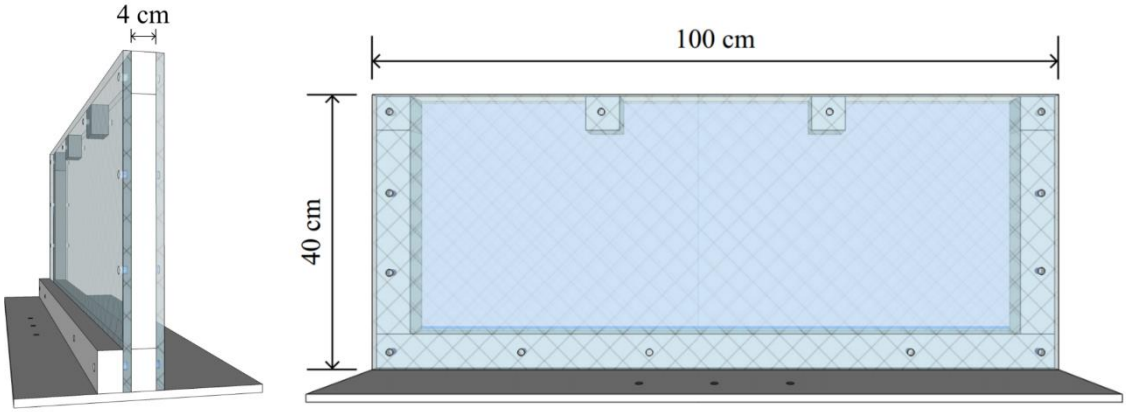

Fig. 3-2 Sketch of channel

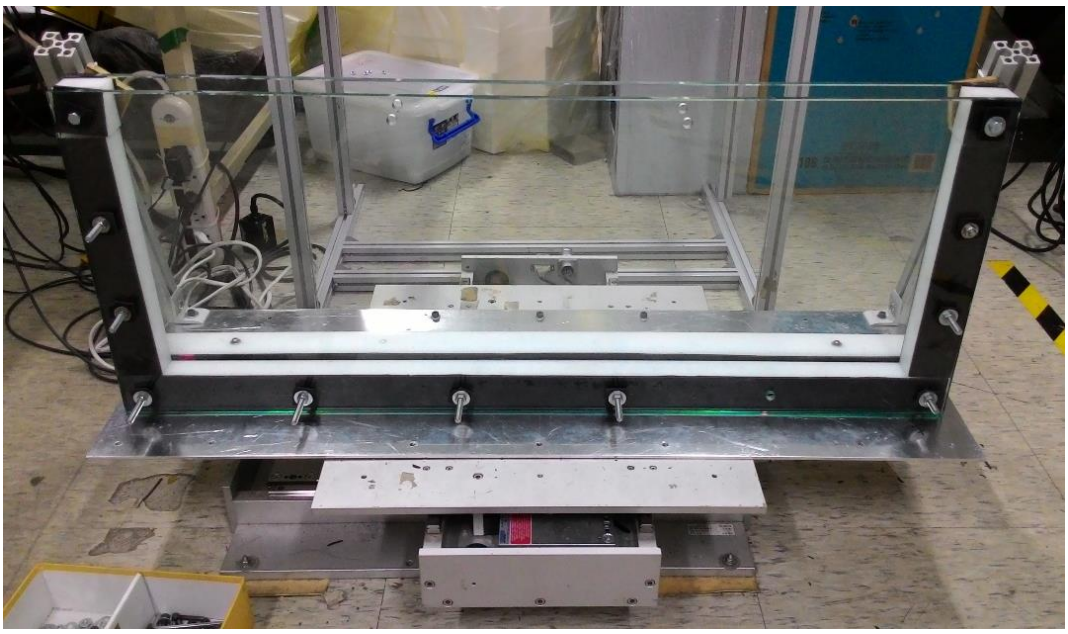

Fig. 3-3 The glass-walled channel

doi:10.6342/NTU201603286

The experiments were performed on the shaking table of the department of civil engineering in National Chiao Tung University. This shaking table has an aluminum alloy platform with a length of 100 cm, width of 120 cm, and is equipped with the screw holes to arrange the specimen (Fig. 3-4). The shaking waveform of experiments is sinusoidal wave. We can set the frequency and amplitude to determine the response of shaking table.

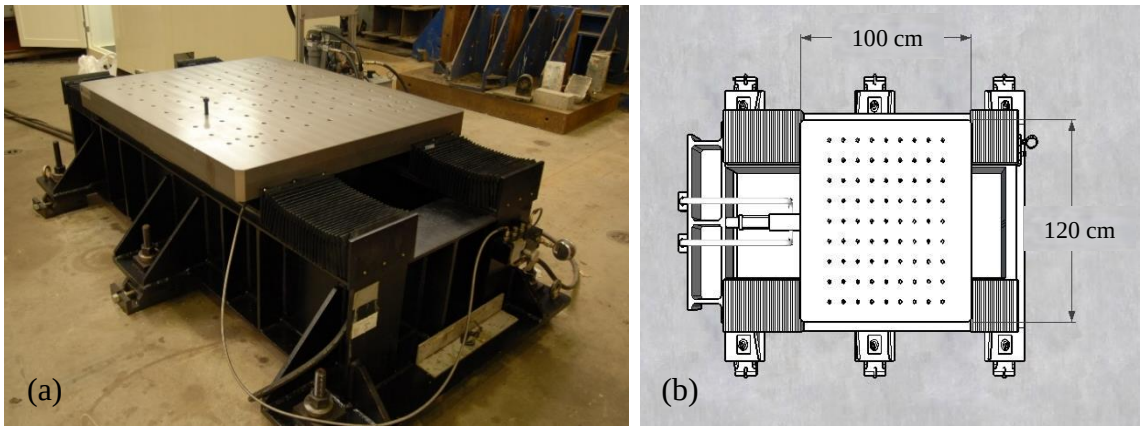

Fig. 3-4 (a) Shaking table (b) Sketch of shaking table

To record the process of experiments and obtain photos which are available for analysis, we use two types of cameras: the high speed camera (HSC) and the digital video (DV). The former is used to capture positions of particles. The frame rates is 200 frames per second and the recording time is about 11 seconds in our experiments. As for the latter, it is used to record the evolution of surface. We operate the digital video to capture the process about 60 seconds.

Fig. 3-5 Image measurement facilities: Digital video

doi:10.6342/NTU201603286

In order to shoot clear photos, we need to lighten the channel. Nonetheless, the light which is supplied by alternating current will flicker on the screen of high speed camera because of the high frame rates. Therefore, we use LED strip which have sufficient brightness and a storage battery to generate the light for experiments (Fig. 3-6 (a)). In addition, the laser line level is used to display an accurately horizontal and vertical line in the experiment (Fig. 3-6 (b)).

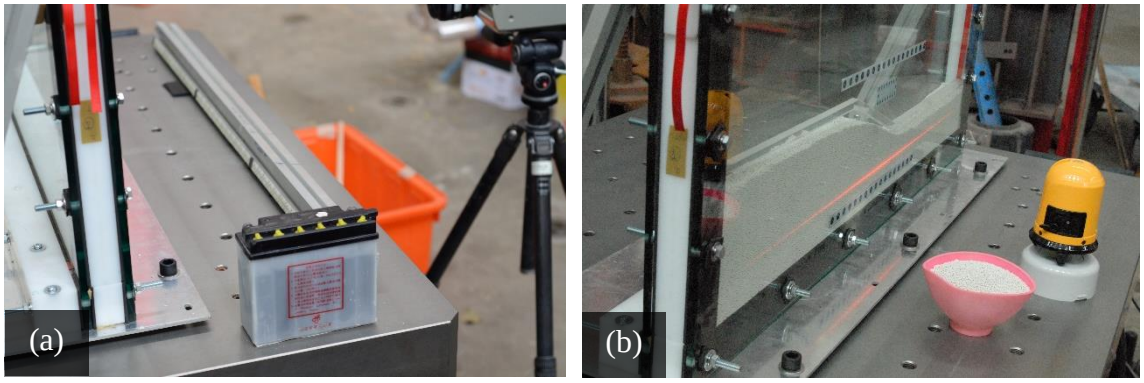

Fig. 3-6 (a) LED strip and battery placed on the platform (b) The laser line level display an accurately horizontal line on the wall

We use glossy mill stones as our experimental material. In order to increase the uniformity of particles and know the particle size, we sift the glossy mill stones through the standard test sieve. The average diameter is 2.3 mm. Since the appearance of particle is easily been observed and the slope can be built successfully by the mill stones, we choose it to be our experimental material.

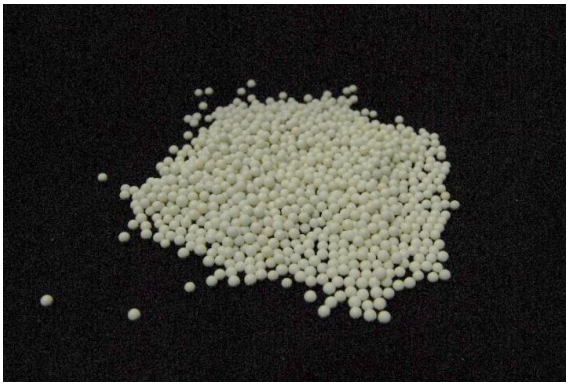

Fig. 3-7 the glossy mill stones used in the experiment

doi:10.6342/NTU201603286

3.2 Experimental procedure

First, we are going to build the slope which reach the critical value. Thus, it is necessary to find the angle of repose of the particles. The channel is divided into two parts, and the particles are piled up with different height. Next, the division plate be drawn out rapidly, and then particles develop a slope naturally. The measurements are carried out several times and recorded by the camera. After that, we analyze the images and use the laser line level which provide the datum to help us calculate the angle. According to the average value, the angle of repose which is the initial angle of our experiment is 22.5 degrees.

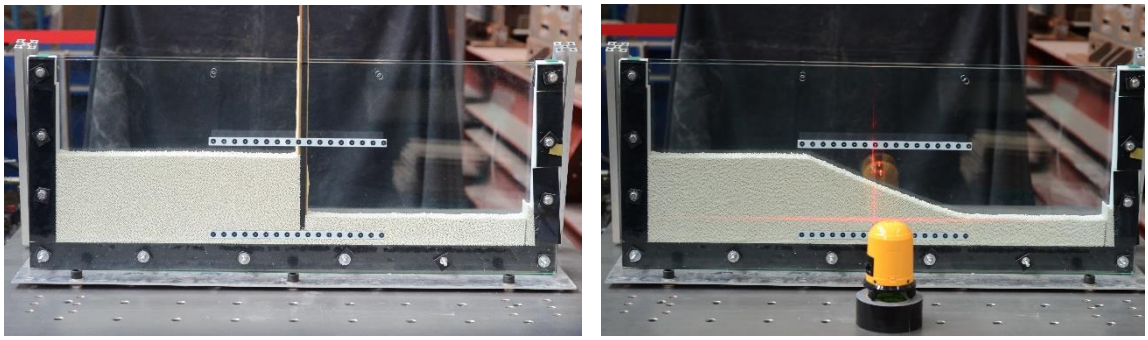

Fig. 3-8 the angle of repose measurements

In order to ensure the repeatability of experiments, we design a frame and a scraper which is made of acrylic to maintain the initial shape of slope (Fig. 3-9 (a)). When we are going to build the slope, the frame is placed on the channel (Fig. 3-9 (b)). Then, the glossy mill stones are poured into the channel through a funnel and the spare particles are scraped away by the scraper (Fig. 3-10). With these procedures, the initial shape of slope is fixed in each experiment.

doi:10.6342/NTU201603286

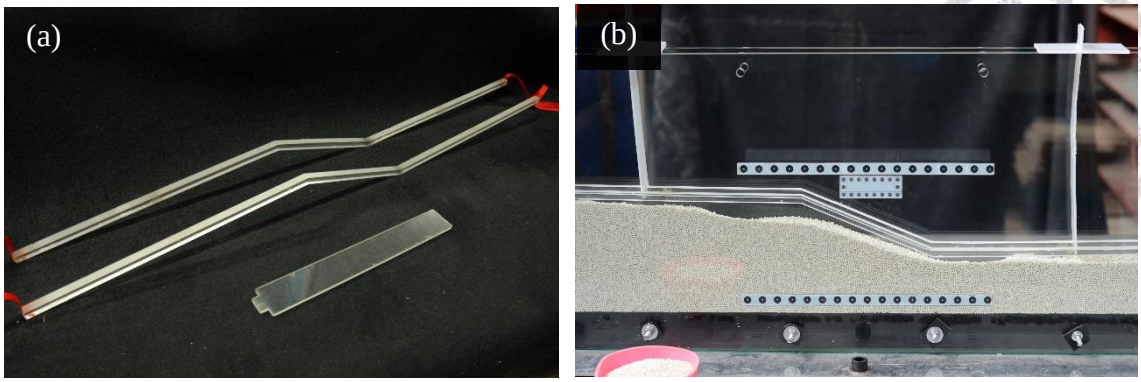

Fig. 3-9 (a) Frame and scraper (b) Frame hung on the channel

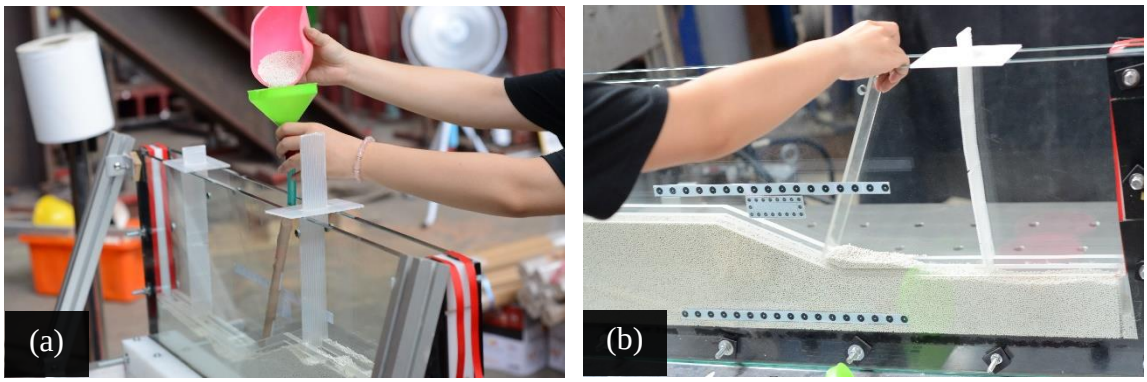

Fig. 3-10 (a) Add particles (b) Scrap the particles

In order to observe the relevance between the slope behavior and the acceleration, we conduct the experiment for 12 rounds under different acceleration and frequency conditions as shown in Table 3.1. From round 1 to round 8, we design 4 different magnitudes of acceleration every two rounds, and the frequency conditions are classified as 4 Hz and 3 Hz. As to the other four rounds, we want to verify the repeatability according to the result of these experiments.

doi:10.6342/NTU201603286

Table 3.1 List of the twelve rounds in shaking table experiment

Round	Frequency (Hz)	maximum acceleration (PTV) (cm/s^2)	maximum acceleration (input) (cm/s^2)
1	3	196.59	230.95
2	4	194.73	252.66
3	3	297.69	348.20
4	4	299.33	378.99
5	3	401.13	454.79
6	4	405.09	492.69
7	3	495.53	575.60
8	4	501.88	619.02
9	3	303.88	355.31
10	3	297.69	348.20
11	3	409.07	461.90
12	3	401.13	454.79

Because of the difference between the input wave and the output wave as shown in Table 3.1, it is difficult for us to keep acceleration the same every time. Moreover, we cannot obtain accurate output acceleration through the input settings. Thus, we measure the output value by PTV method, which we will introduce in the next section. With the PTV results, we can discover the noise in the acceleration signal (Fig. 3-11), hence we use the least squares method to fit the data obtained by PTV analysis to define the maximum acceleration in each round. We use Gauss–Newton method to solve the least squares problems, and the model function is defined as below:

$$y = a\sin(bt + c) \tag{2.55}$$

Since the vibration is unstable in first period, the data is not used in fitting. According to the fitting result, the maximum acceleration of our experiments can be defined. We take round 6 for example. In Fig. 3-11, the results are plotted together, and we can determine the maximum acceleration of round 6 is 297.69 cm/s^2 by the equation.

doi:10.6342/NTU201603286

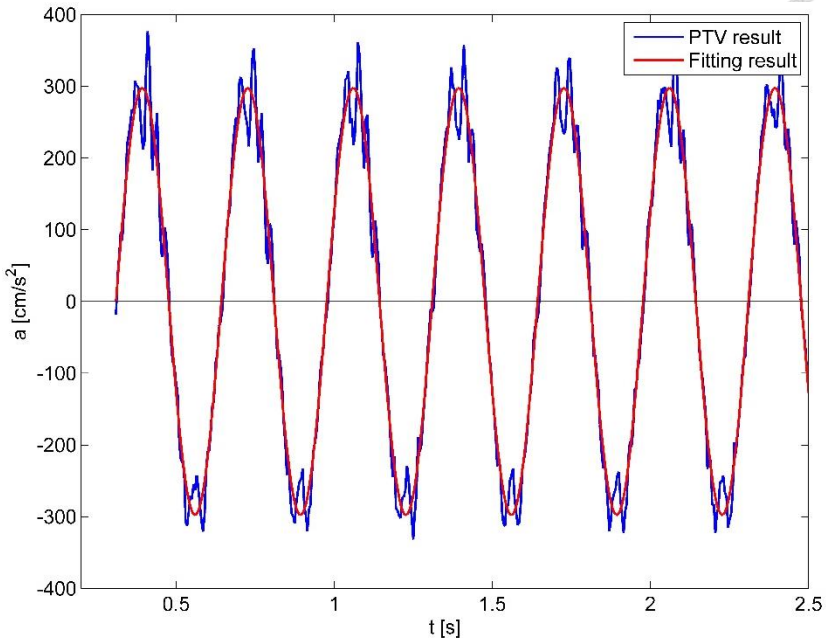

Fig. 3-11 Fitting acceleration at round 6: the equation of fitting result is $y = 297.69\sin(18.85t + 0.4414)$

There are three different sizes of observation regions which is illustrated in Fig. 3-12 in this study. Region A focus on the center of slope to analyze the velocity profile of particles. As to region B, we want to observe the slip surface. Then, the digital video records region C to capture the surface deformations.

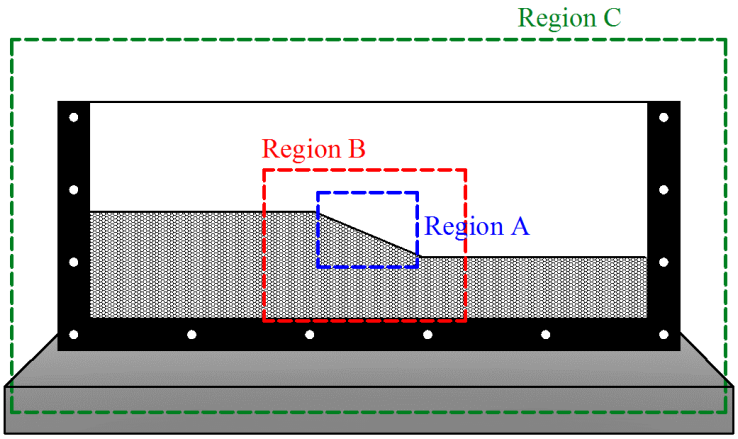

Fig. 3-12 Three different observation regions

doi:10.6342/NTU201603286

3.3 Image method

3.3.1 Calibration

Since the photos are in pixel coordinates, we need to transform the coordinates system from image coordinates to real world coordinates first. In order to obtain the relation between these two systems, the calibration points are put on the wall of the channel. According to the different observation regions, we design three different size calibration points as shown in Fig. 3-13.

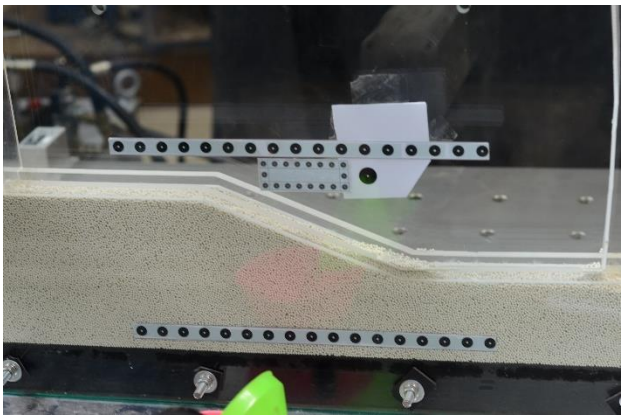

Fig. 3-13 The calibration points which we used in the experiment

3.3.2 Image pre-processing

Before applying the PTV method, we need to adjust the photos first. Since the high speed camera is located on the ground rather than move with the shaking table, it is necessary to remove the displacement of each photos before computing the velocity of particles. The position of channel at each moment can be obtained by capturing the calibration points. Then, we use the data to calculate the displacement and velocity of shaking table, and the results also enable us to divide the photos into each period. In Fig. 3-14, we take two photos in the same period as example. The calibration points move with the shaking table in original photos. After we transform the coordinate and remove

doi:10.6342/NTU201603286

the displacement, the photos seem to be taken by the camera which is placed on the shaking table. The adjusted photos have no extra movement, so they are able to further analyze.

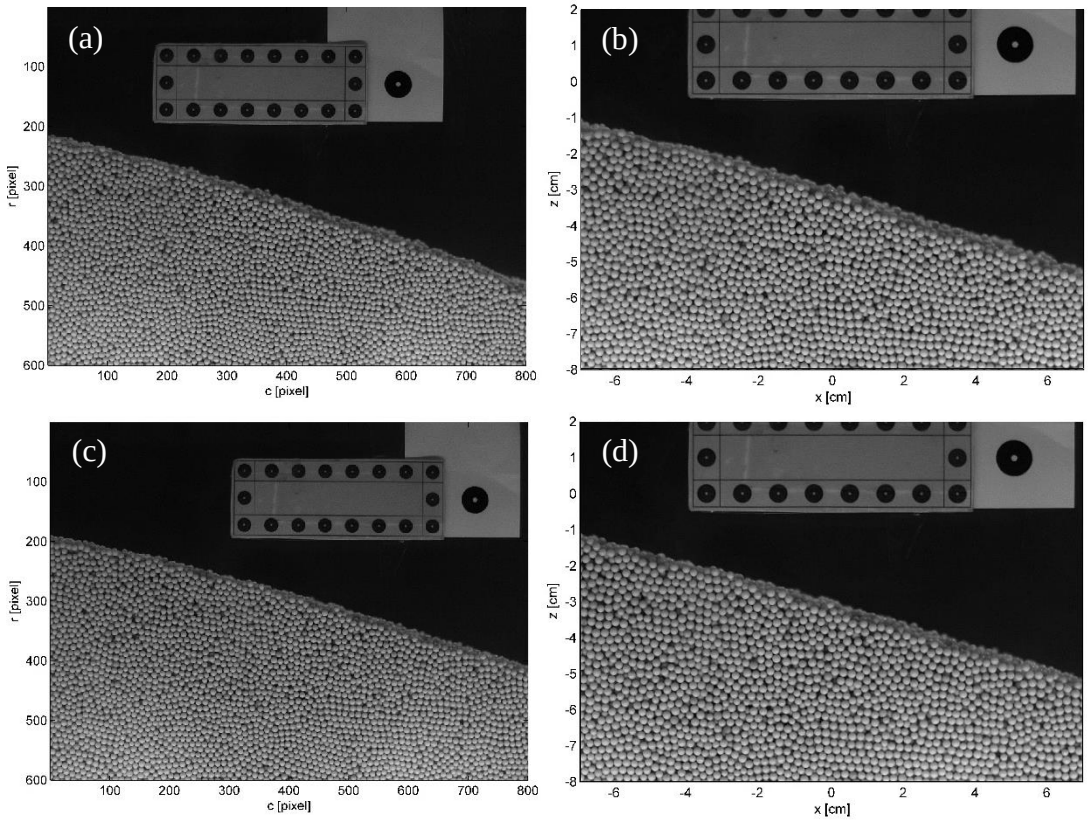

Fig. 3-14 Photo rectification: (a) original photos and (b) rectified images in the beginning of a period; (c) original photos and (d) rectified images in the interval of a period.

When observing the region A, it means that we focus on the velocity profile of the slope. Thus, we rotate the images to let slope be parallel to the horizontal with rotation matrix.

$$R = \begin{bmatrix} \cos\theta & \sin\theta \\ -\sin\theta & \cos\theta \end{bmatrix} \tag{2.56}$$

$$\begin{bmatrix} x' \\ y' \end{bmatrix} = R \begin{bmatrix} x \\ y \end{bmatrix} = \begin{bmatrix} \cos\theta & \sin\theta \\ -\sin\theta & \cos\theta \end{bmatrix} \begin{bmatrix} x \\ y \end{bmatrix} \tag{2.57}$$

doi:10.6342/NTU201603286

Where (x', y') is the point in new coordinate system, R is the rotation matrix, θ is the slope of photos, and (x, y) is the point in original coordinate system.

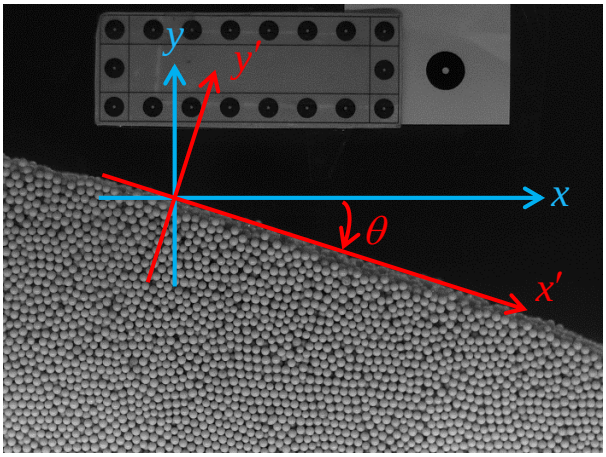

Fig. 3-15 original coordinate system (red lines) and new coordinate system (blue lines)

3.4 Verification

3.4.1 Image method applicability

To verify the PTV method can be applied to track the movement and velocity of shaking table, we compare the actual performances of shaking table experiments with the data from PTV analysis. The response of shaking can be obtained by some devices. The linear variable displacement transducer (LVDT) and the accelerometer mounted on the platform (Fig. 3-16) measure the displacement and acceleration outputs. We take round 2 as an example to plot the position and acceleration as shown in Fig. 3-17 and Fig. 3-18. It is observed that PTV results match well with the position feedback (LVDT), and the acceleration obtained from PTV analysis has a similar trend with the accelerometer signals.

doi:10.6342/NTU201603286

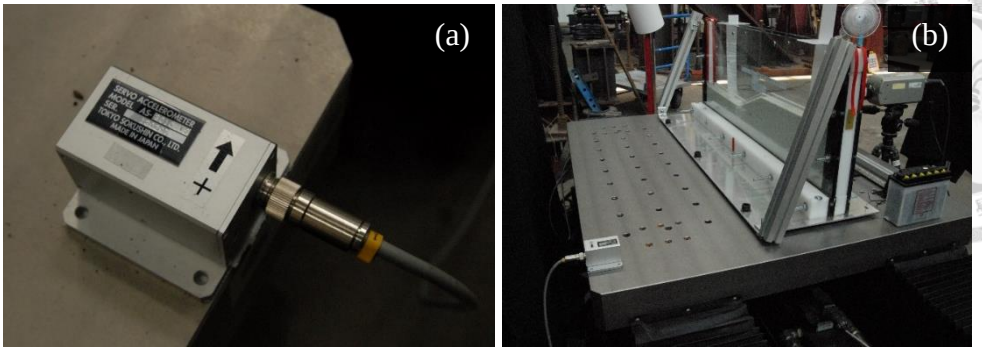

Fig. 3-16 (a) Accelerometer (b) Arrangement of the accelerometer

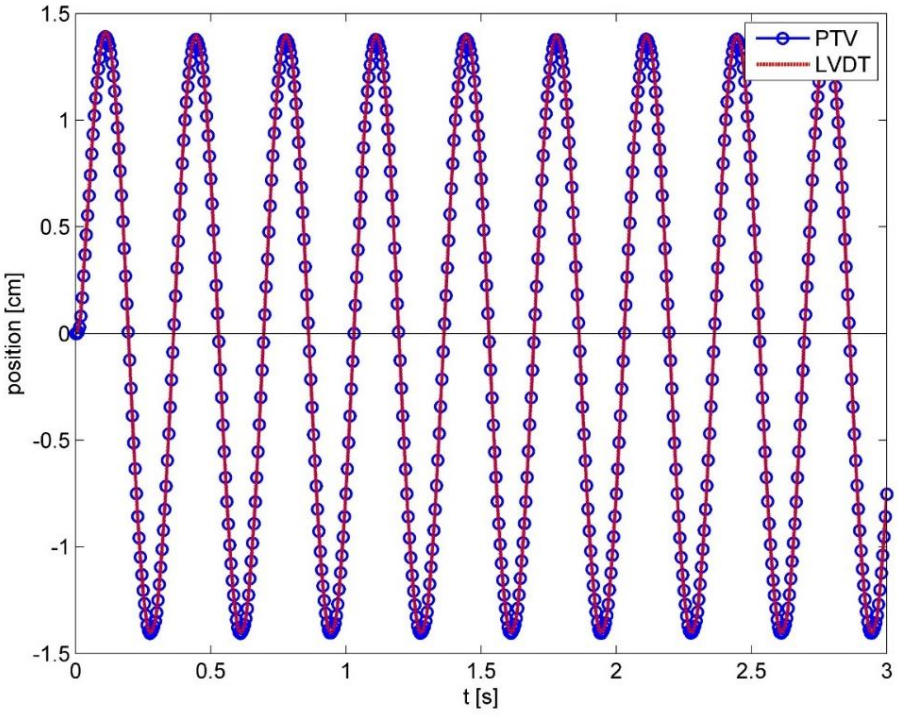

Fig. 3-17 Position of the shaking table at round 2

doi:10.6342/NTU201603286

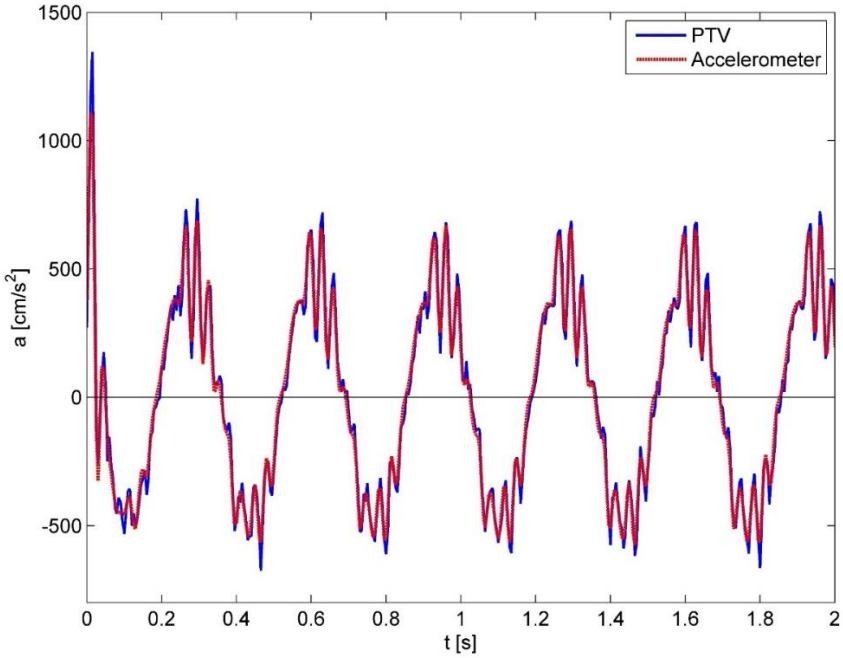

Fig. 3-18 Acceleration signal of the shaking table at round 2

We use the photos which are transformed into real world coordinates to plot the time exposure image. As can be seen in Fig. 3-19, the calibration points and the deeper particle are seen clearly. This result means that not only are they static relative to the channel, but also the procedure for removing the displacement from images is practicable. These results indicate that PTV analysis is available to capture the movement of shaking table and transform the coordinates system of images.

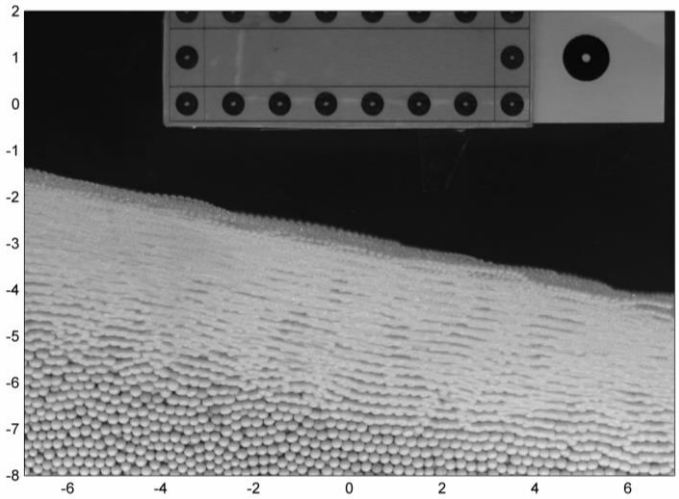

Fig. 3-19 Time exposure image of third period at round 2

doi:10.6342/NTU201603286

3.4.2 Repeatability

In order to enhance the credibility of our experimental results, we need to confirm the behavior of particles is similar under same conditions. As we mentioned in the previous section, two sets of experiments are performed to verify the repeatability of experiments. We analyze the slip range, velocity magnitude and the variance of slope of each case. The comparison is plot from Fig. 3-20 to Fig. 3-22. We can observe that the experiments under same conditions have good repeatability.

doi:10.6342/NTU201603286

Round 9	Round 10

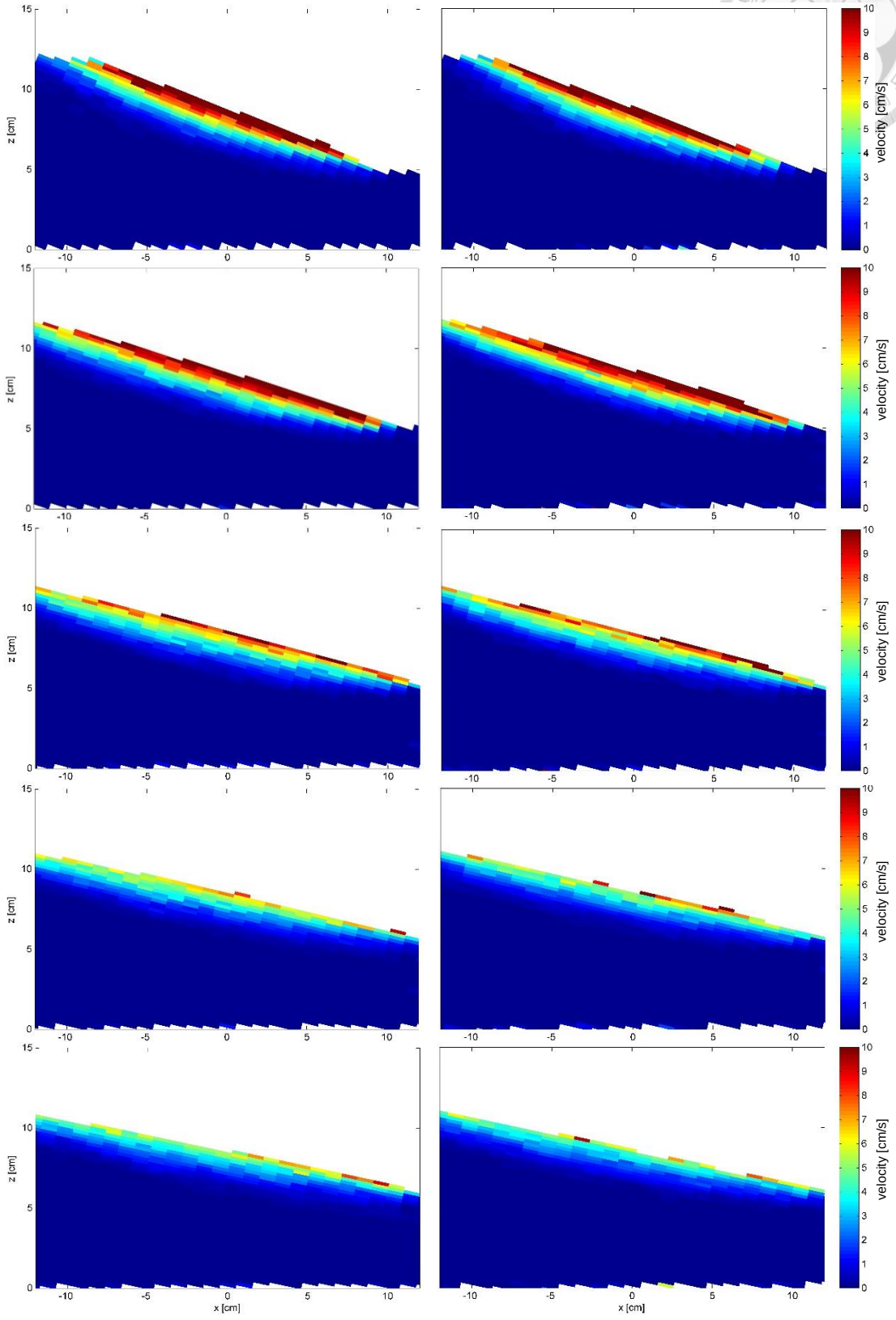

Fig. 3-20 Mean flow velocity magnitude of round 9 and round 10

doi:10.6342/NTU201603286

Round 11	Round 12

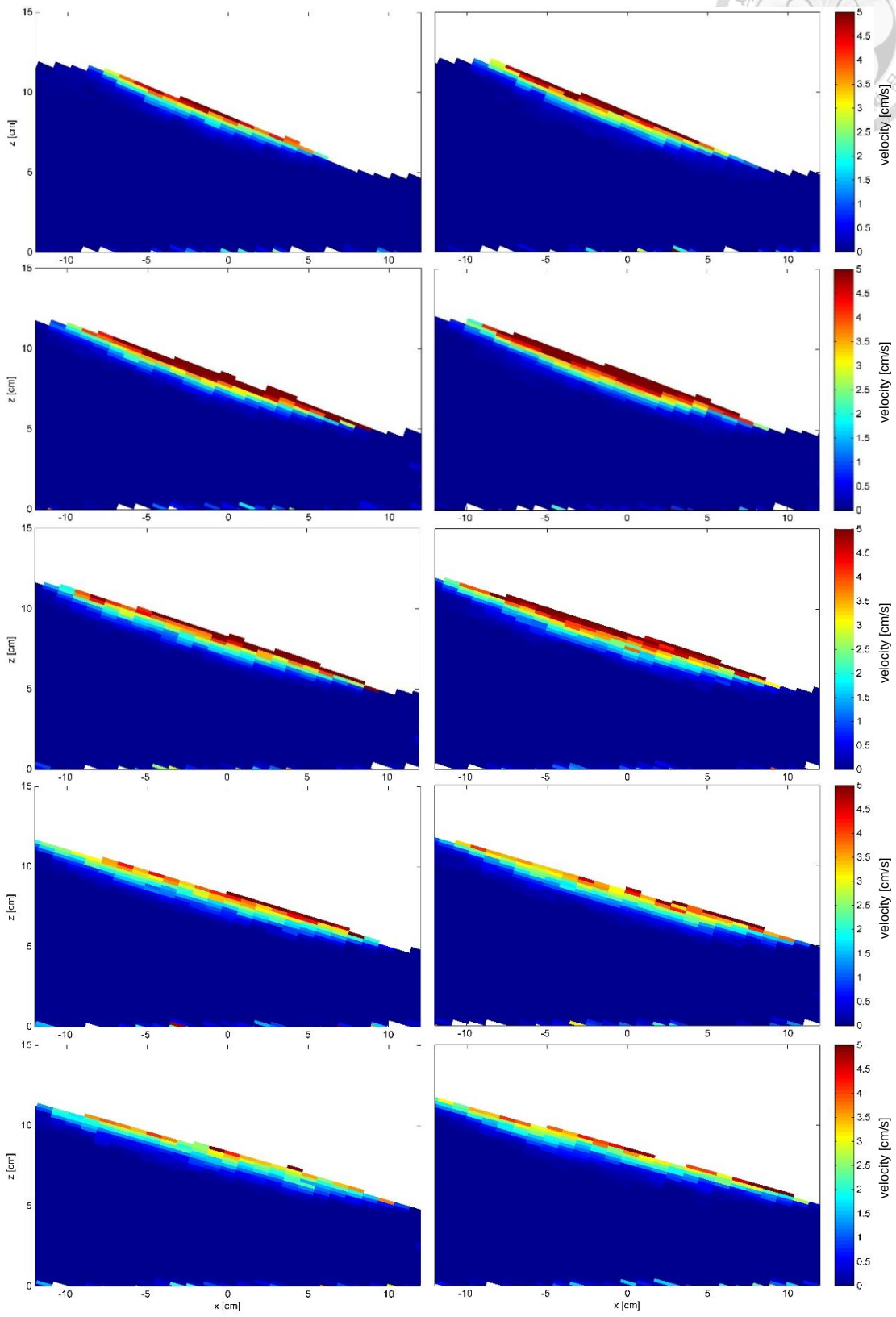

Fig. 3-21 Mean flow velocity magnitude of round 11 and round 12

doi:10.6342/NTU201603286

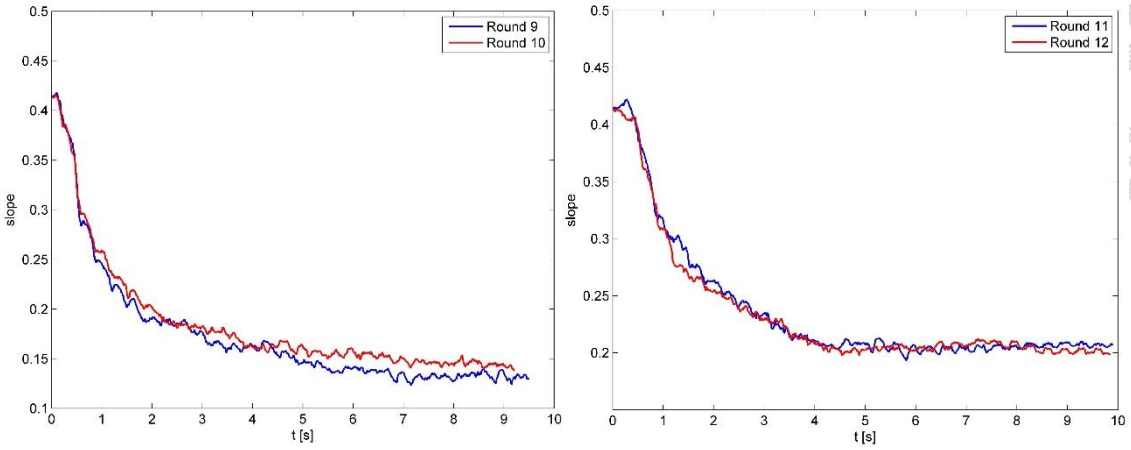

Fig. 3-22 The variance of slope under similar conditions

doi:10.6342/NTU201603286

Chapter 4 Results and comparison

The analysis results of our experiments are shown in this chapter. We put the mean flow velocity magnitude of each round together. Based on the PTV data, we can acquire the time-evolving variables and compare the results with theory which we derivate in previous chapter. In the process of analysis, not only the observation region but also the time scale of analysis is not fixed in our experiment because of the different object. We observe the average velocity field of each period and divide period into 8 sections to find the behavior of particles within the period. The detailed classification is shown in Fig. 4-1.

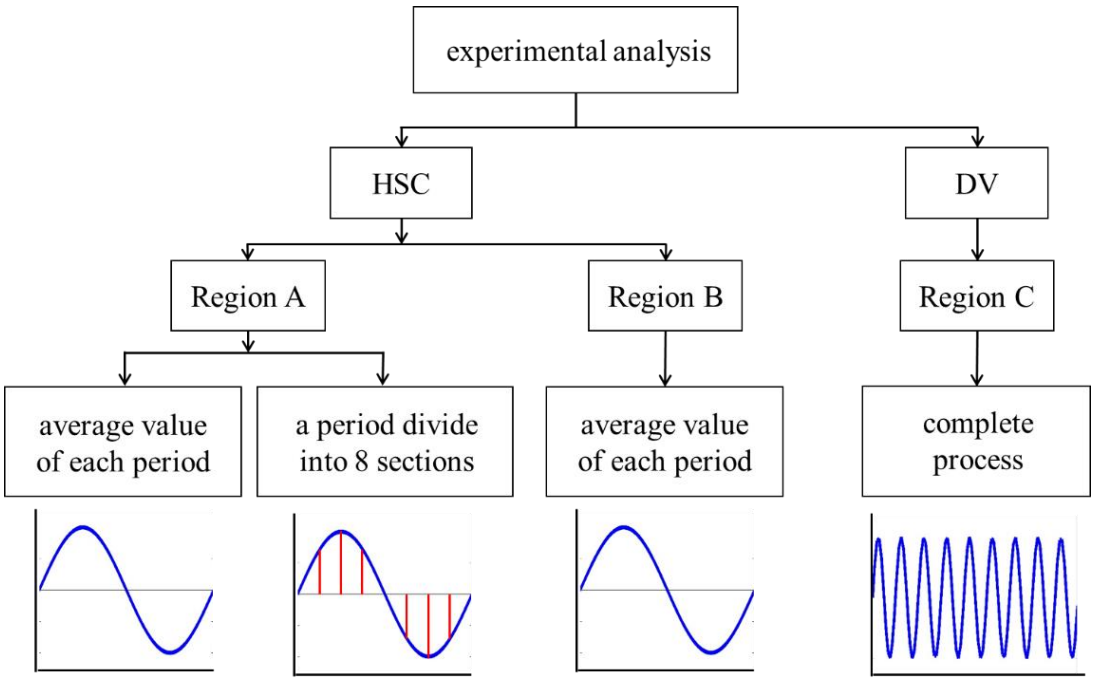

Fig. 4-1 Classification of experimental analysis with different time scale

doi:10.6342/NTU201603286

4.1 Granular velocity fields

The velocity field of slip surface can be captured by PTV method. In Fig. 4-2 and Fig. 4-3, the time exposure images are compared with the mean velocity magnitude images. We can observe that the flowing layer is similar among these two image analysis methods. From Fig. 4-4 to Fig. 4-6, we draw a comparison between different frequency from first period to fifth period. The results show that the case which frequency is 3 Hz reach higher velocity faster and the slip depth is deeper than the case which frequency is 4 Hz.

doi:10.6342/NTU201603286

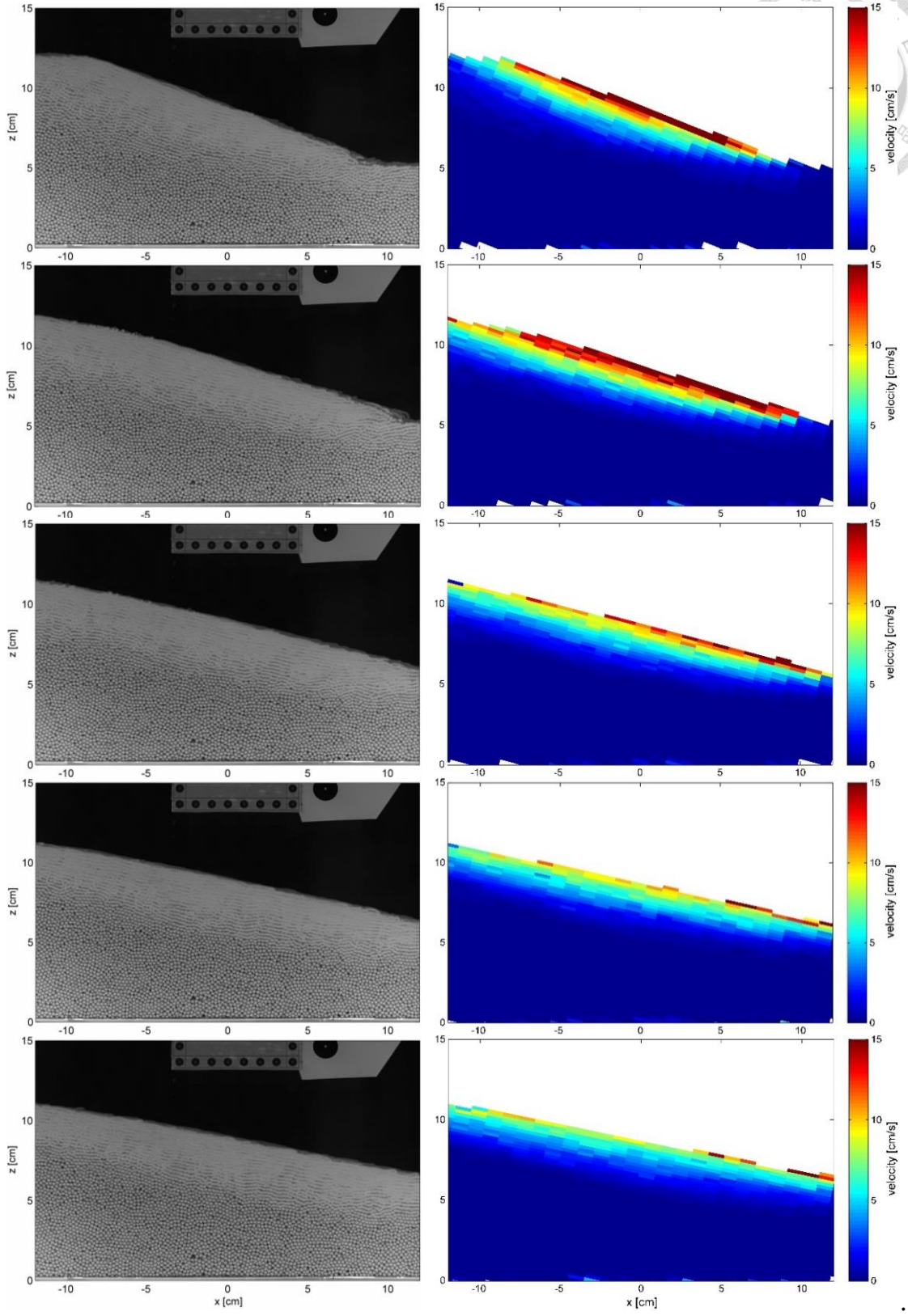

Fig. 4-2　Time exposure and mean velocity magnitude images from period 1 to period 5 of round 1

doi:10.6342/NTU201603286

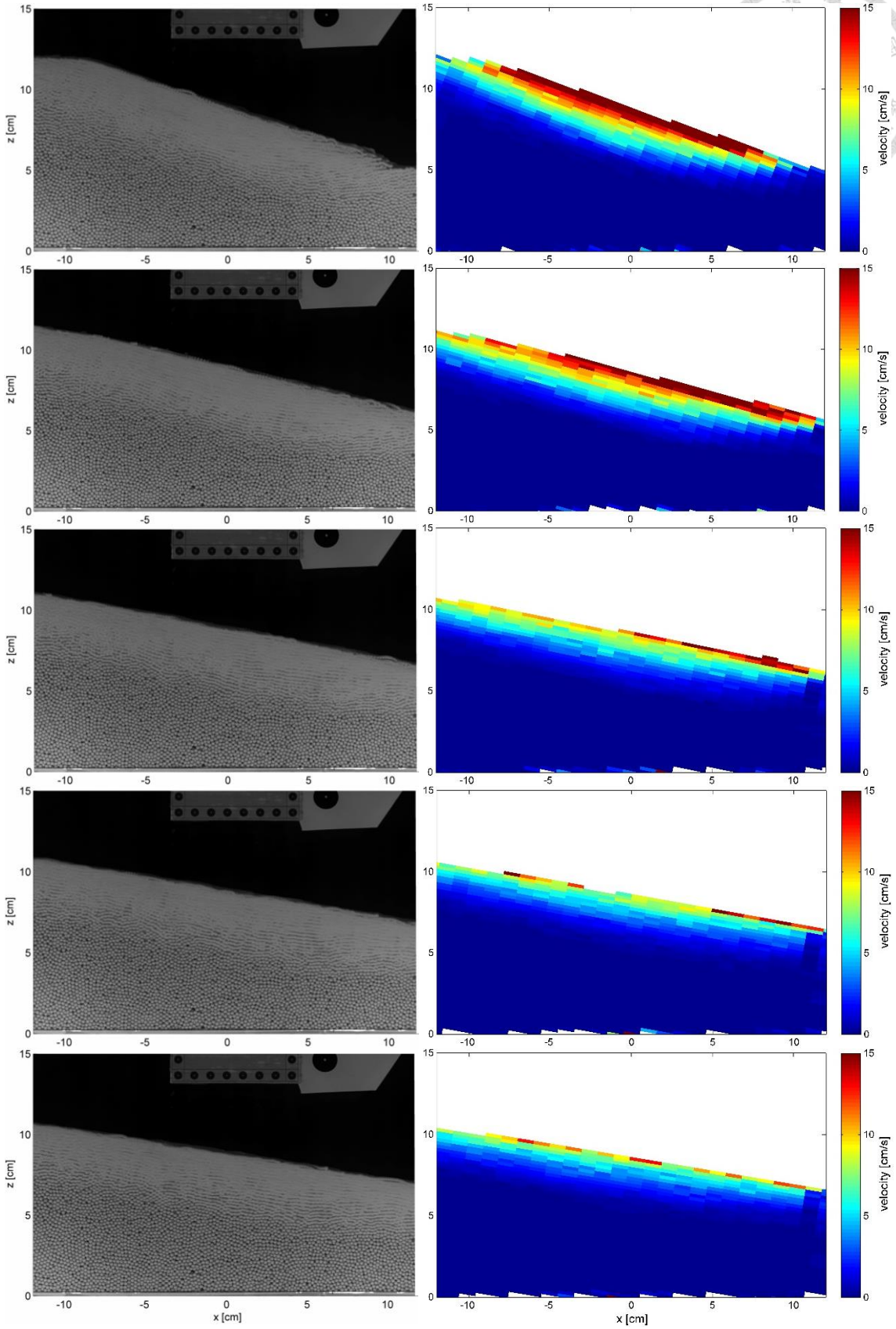

Fig. 4-3 Time exposure and mean velocity magnitude images from period 1 to period 5 of round 2

doi:10.6342/NTU201603286

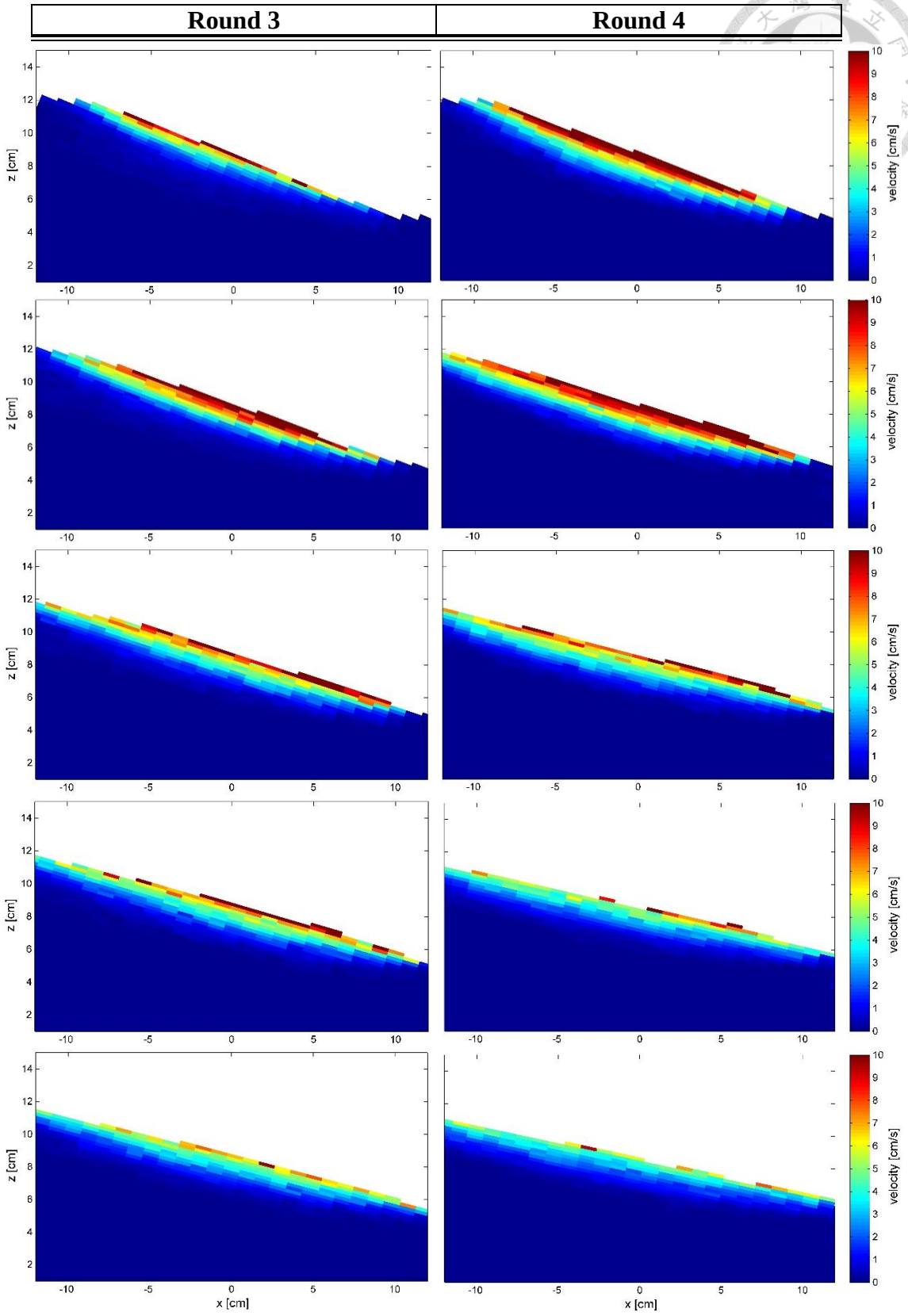

Fig. 4-4 Mean velocity magnitude images from period 1 to period 5 of round 3 and round 4.

doi:10.6342/NTU201603286

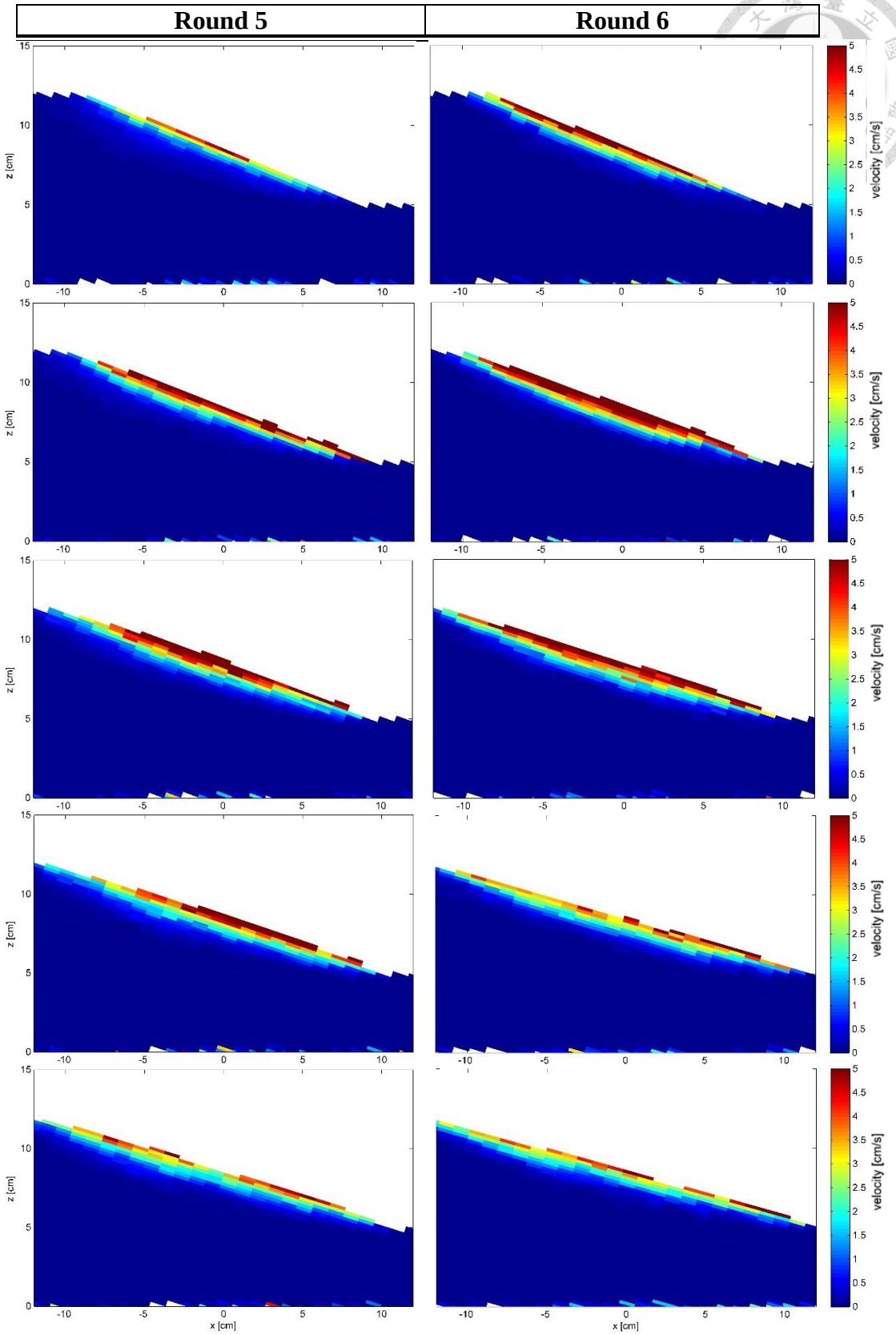

Fig. 4-5 Mean velocity magnitude images from period 1 to period 5 of round 5 and round 6.

doi:10.6342/NTU201603286

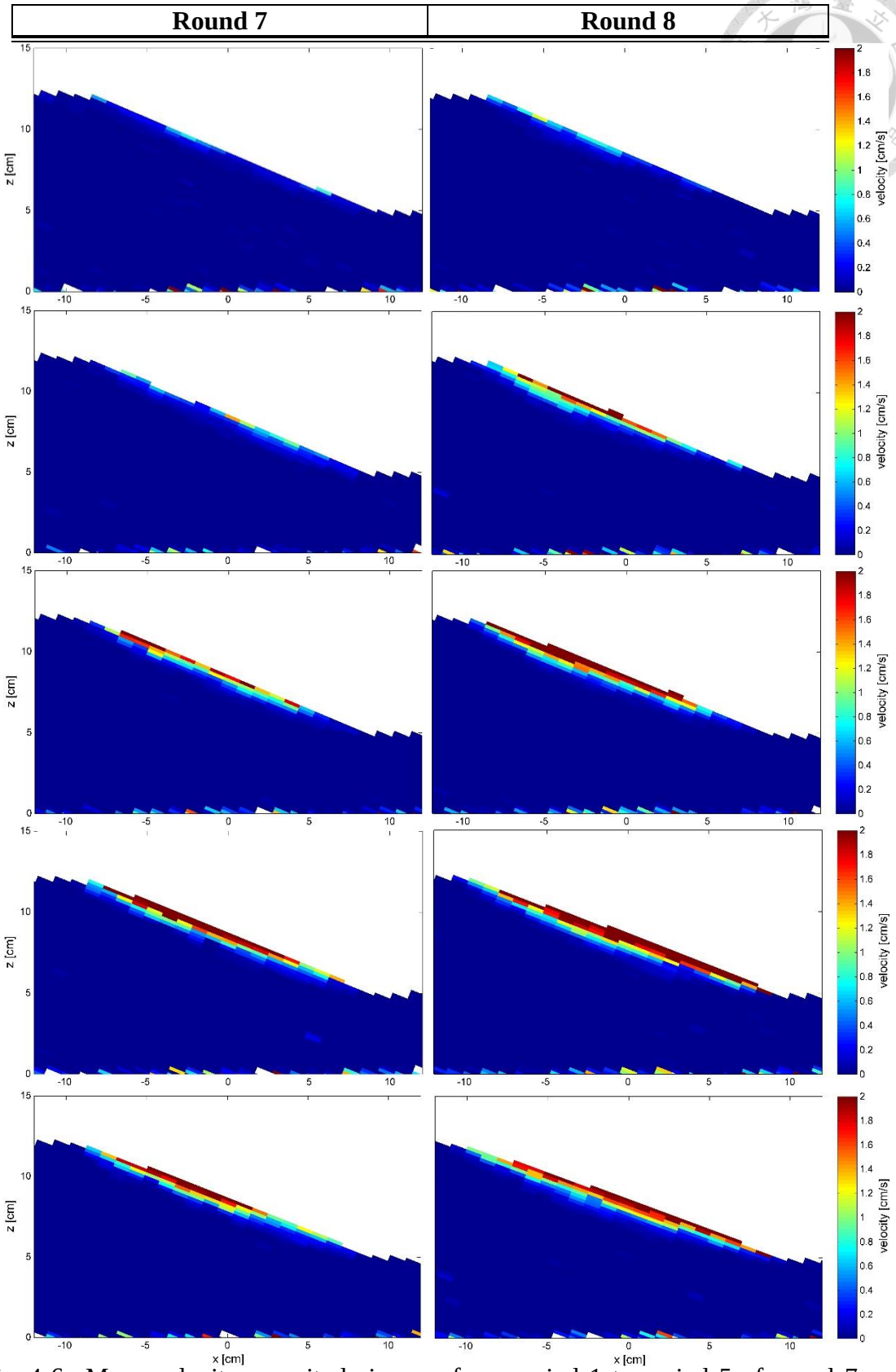

Fig. 4-6 Mean velocity magnitude images from period 1 to period 5 of round 7 and round 8.

doi:10.6342/NTU201603286

4.2 Time-evolving variables

In addition to the velocity field, we are interested in the time-evolving variables. We can obtain the flux, velocity profile, and maximum velocity by PTV data. Flux is the flow rate per unit width, and be calculated by the equation:

$$q(t) = \int_0^{\tilde{z}} u dz \tag{4.1}$$

Additionally, we can plot the surface shape and acquire the time-evolving surface slope with the photos recorded by digital video. These variables are showed from Fig. 4-7 to Fig. 4-12. In order to distinguish each round easily, we plot the data with specified color, which is set according to the magnitude of acceleration, and the corresponded color scale is also shown on the figure. As mentioned in the beginning of this chapter, the analysis can divide into three different time scales. In the part of flux and maximum velocity calculation, the results can be classified into the mean value of each period and the value of each sections. We can observe the variation of flux and maximum velocity with time in Fig. 4-7, and the value decrease gradually. The periodic variation of flux and maximum velocity is shown in Fig. 4-8 and Fig. 4-9 . We find that the flux and velocity are negative during a portion of a period. In addition, the variation of slope is recorded by the digital video, and the results are plotted in Fig. 4-10. We can use this data to obtain the equilibrium angle $\tan\beta_c$ after the shaking motion.

doi:10.6342/NTU201603286

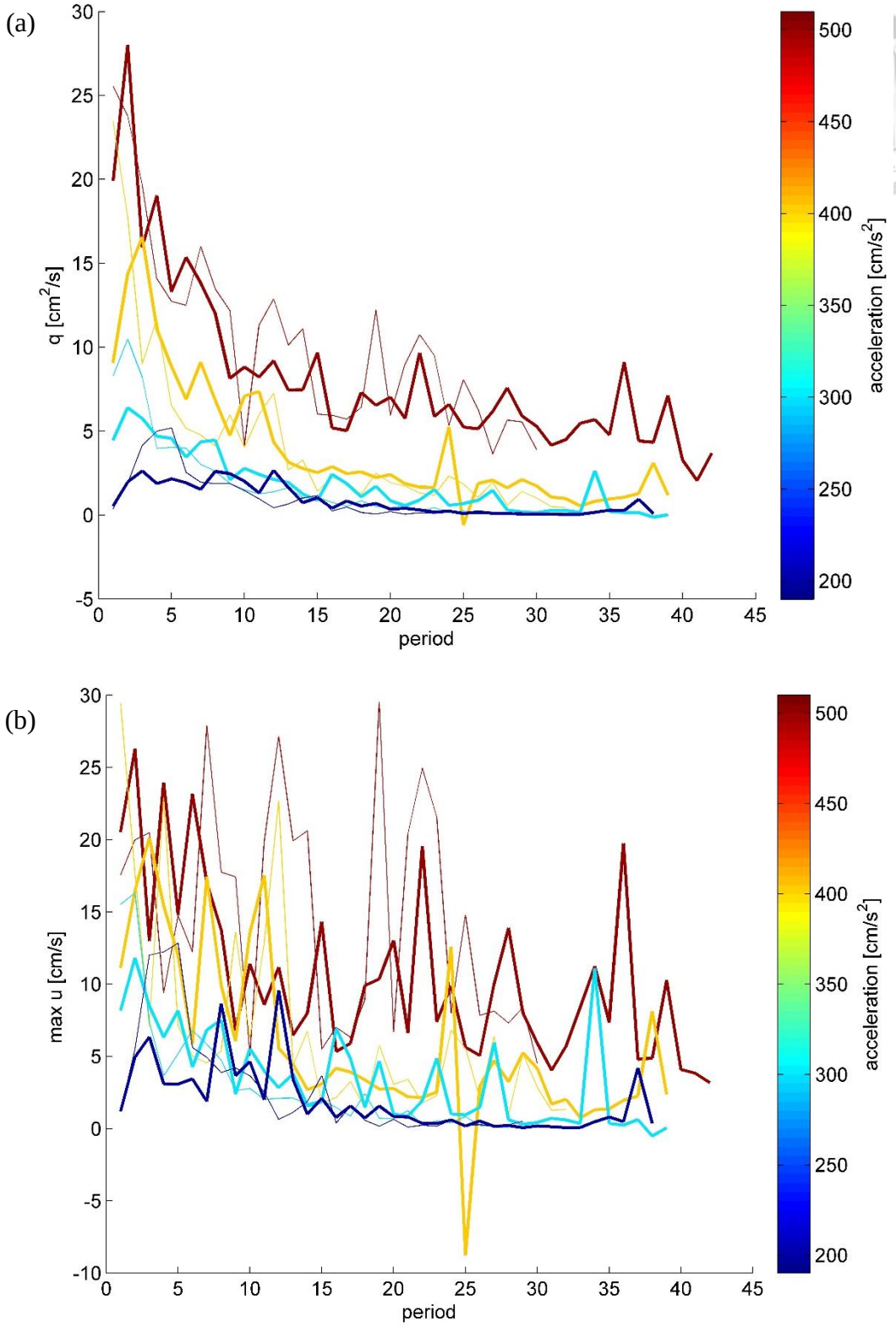

Fig. 4-7 (a) Average value of flux q in each period. (b) Maximum velocity in each period. The bold lines are frequency $= 4Hz$, the thin lines are frequency $= 3Hz$, and the color represents different accelerations.

doi:10.6342/NTU201603286

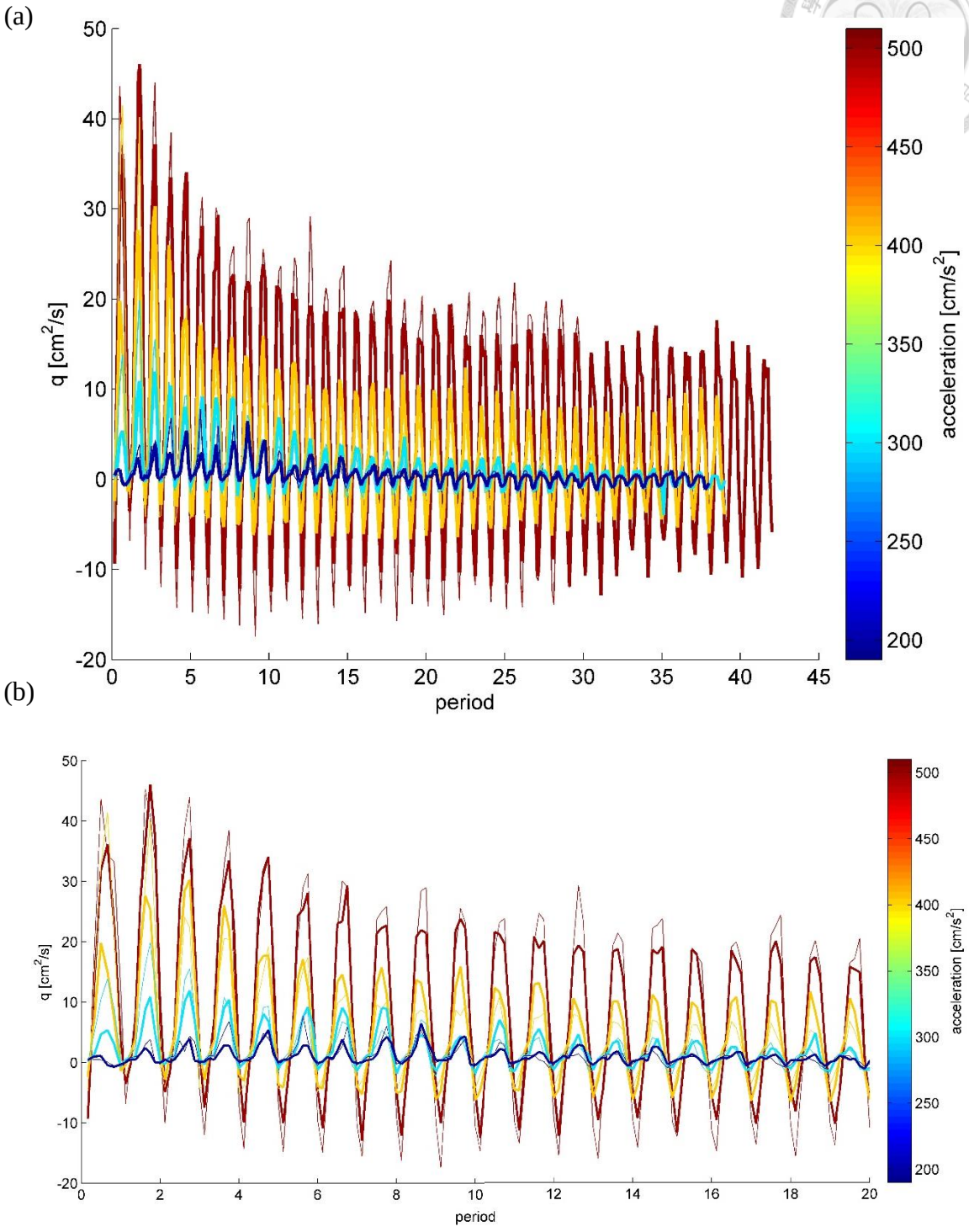

Fig. 4-8 Time evolution of flux q (a) within the whole recording time; (b) zoom in on the time axis. The bold lines are frequency $= 4Hz$, the thin lines are frequency $= 3Hz$, and the color represents different accelerations.

doi:10.6342/NTU201603286

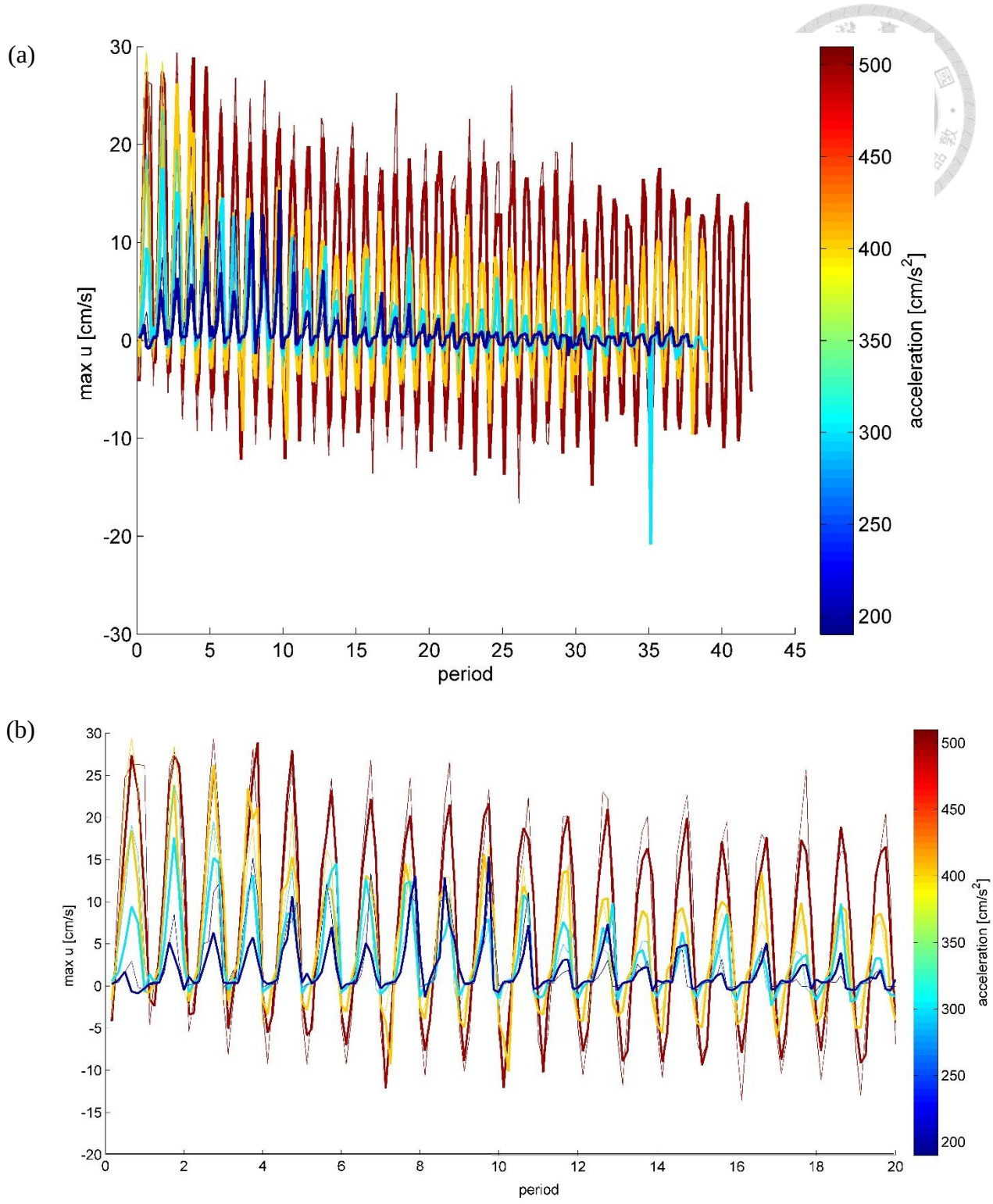

Fig. 4-9 Time evolution of maximum velocity (a) within the whole recording time; (b) zoom in on the time axis. The bold lines are frequency $= 4Hz$, the thin lines are frequency $= 3Hz$, and the color represents different accelerations.

doi:10.6342/NTU201603286

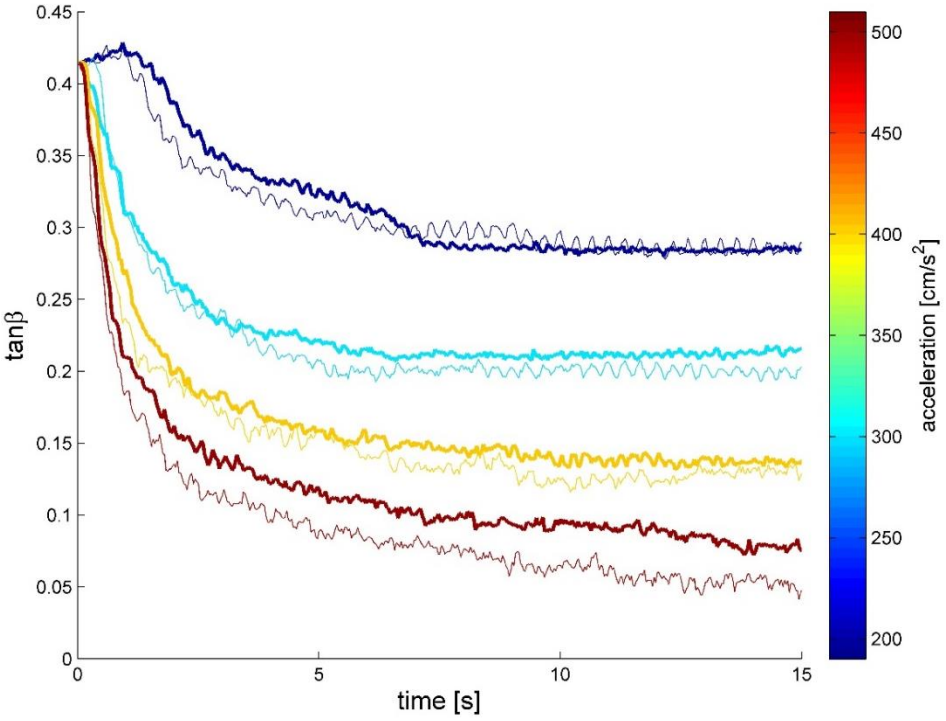

Fig. 4-10 Time evolution of surface slope. The bold lines are frequency = 4*Hz* , the thin lines are frequency = 3*Hz* , and the color represents different accelerations.

doi:10.6342/NTU201603286

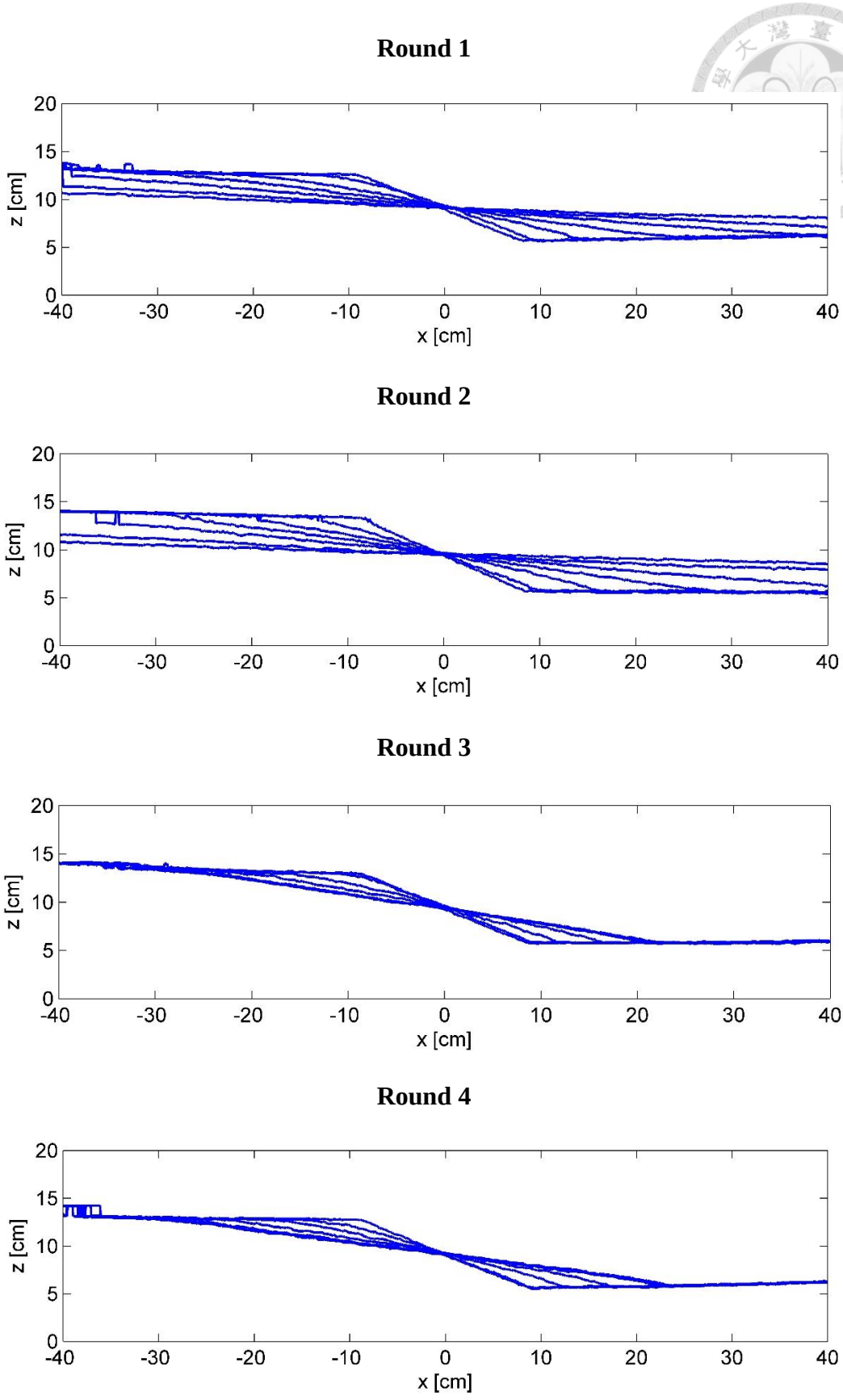

Fig. 4-11 The surface shape of round 1 to round 4 at $t = 0,\ 0.3,\ 1,\ 3,\ 10,\ 30,\ 60$ sec.

doi:10.6342/NTU201603286

Round 5

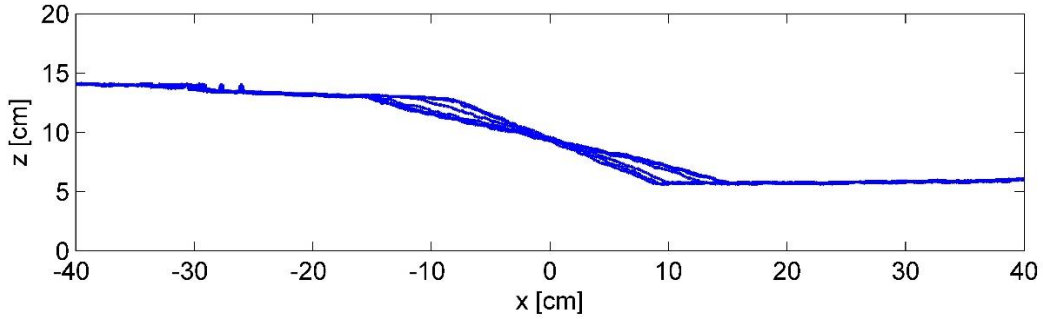

Round 6

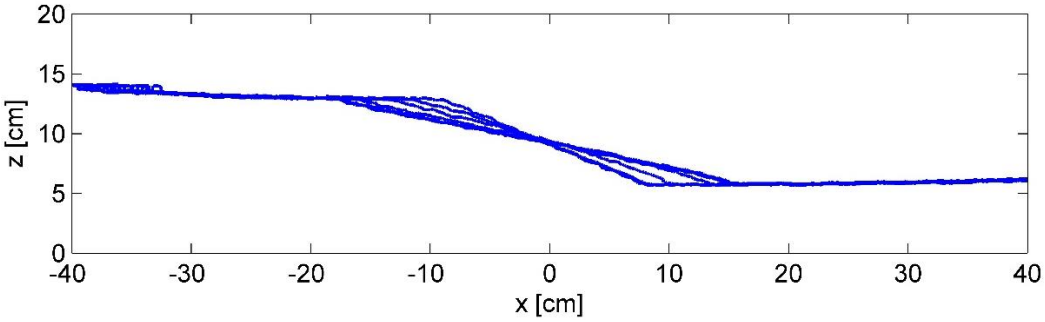

Round 7

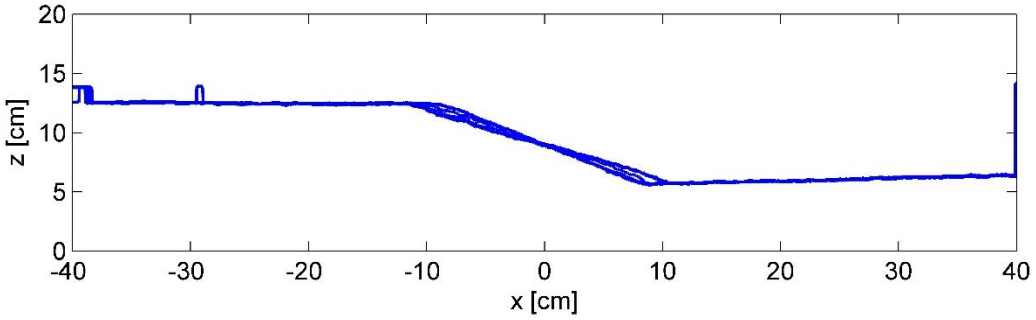

Round 8

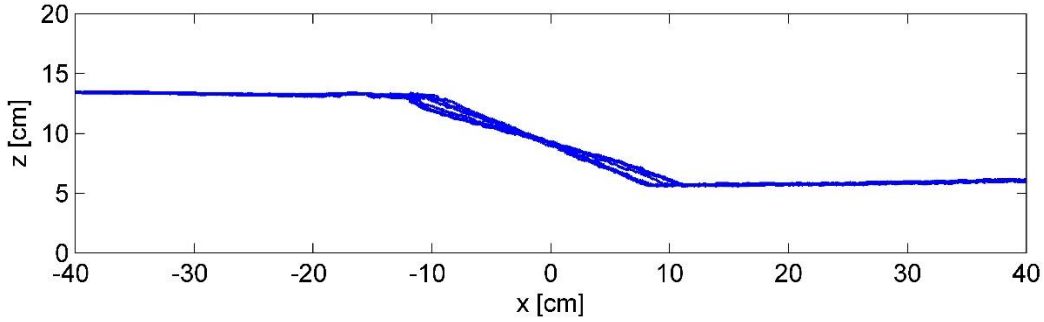

Fig. 4-12 The surface shape of round 5 to round 8 at $t = 0,\ 0.3,\ 1,\ 3,\ 10,\ 30,\ 60$ sec.

doi:10.6342/NTU201603286

4.3 Relation between slope and flux

Based on the results of theory and experiment, we can find the relation of slope and flux, and compare these two methods. The result of $\tan\beta$ and flux measured from experiments is shown in Fig. 4-13. Then, we substitute the experiment data into equation (2.38), and we get the $\alpha = 28.03°$ as shown in Fig. 4-14. Thus, we substitute two kinds of angle of repose into the theory, and compare with the experiment data. We consider the original theory which acceleration is a sinusoidal wave and the semi-analytical solution which acceleration is a parabola. The results of sinusoidal wave accelerations are plotted in Fig. 4-17 and Fig. 4-16. The results of semi-analytical solution are plotted in Fig. 4-17 and Fig. 4-18. We can observe the trend is similar between the theory and experiment in the case of $\alpha = 22.5°$.

doi:10.6342/NTU201603286

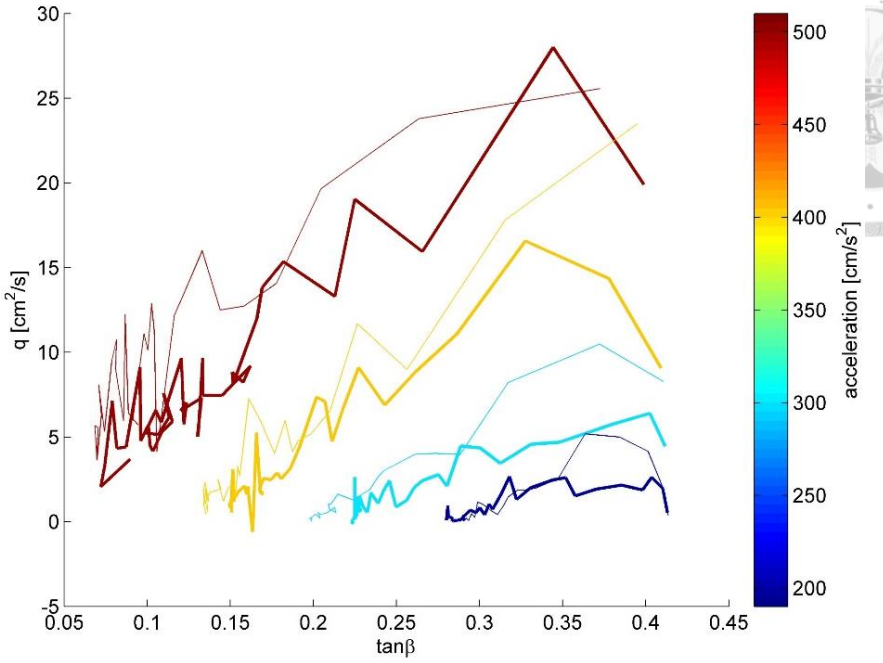

Fig. 4-13 The relation of $\tan\beta$ and flux measured from experiments. The bold lines are frequency $= 4Hz$, the thin lines are frequency $= 3Hz$, and the color represents different accelerations.

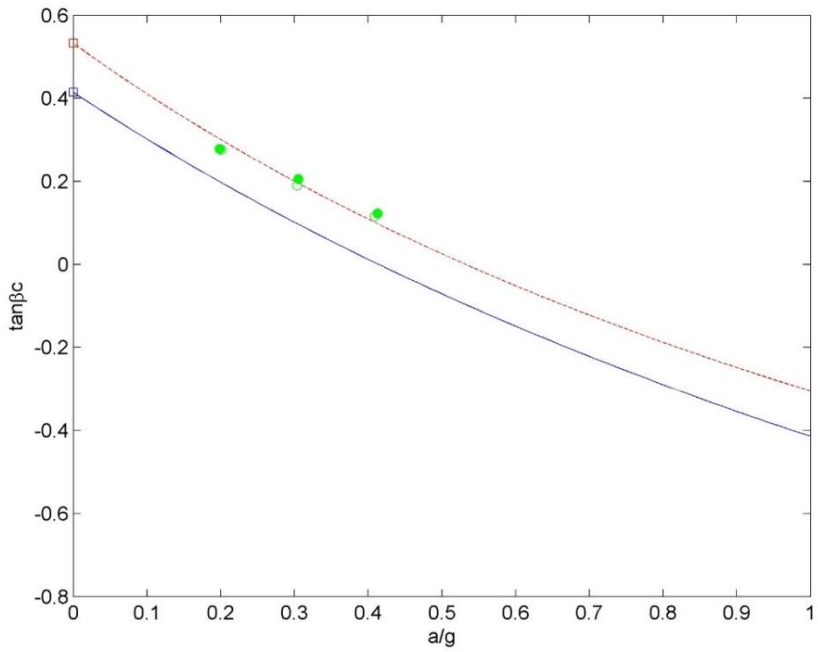

Fig. 4-14 The relation of acceleration and $\tan\beta_c$. The red dotted line is $\alpha = 28.03°$, the blue lines is $\alpha = 22.5°$, and the green points are experiment data.

doi:10.6342/NTU201603286

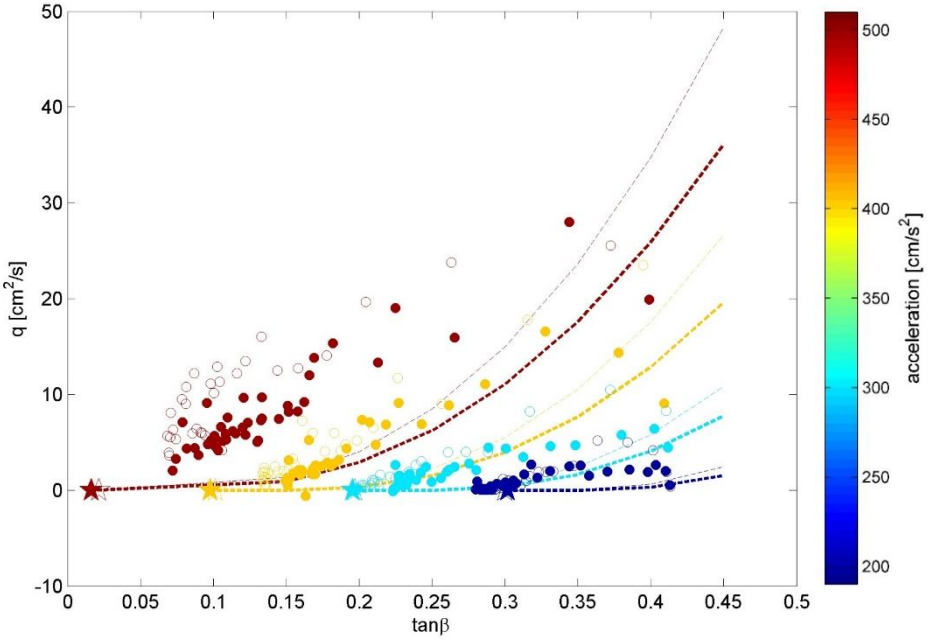

Fig. 4-15 The relation of $\tan\beta$ and flux with $\alpha = 28.03°$. The color dotted lines are theoretical results, the points are experiment data, the bold lines are frequency $= 4Hz$, the thin lines are frequency $= 3Hz$, and the color represents different accelerations.

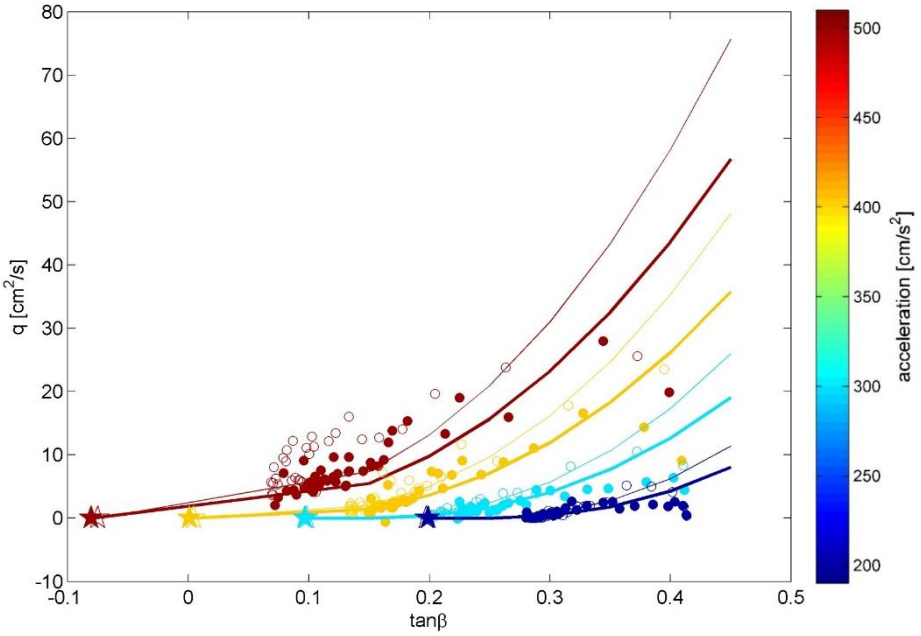

Fig. 4-16 The relation of $\tan\beta$ and flux with $\alpha = 22.5°$. The color lines are theoretical results, the points are experiment data, the bold lines are frequency $= 4Hz$, the thin lines are frequency $= 3Hz$, and the color represents different accelerations.

doi:10.6342/NTU201603286

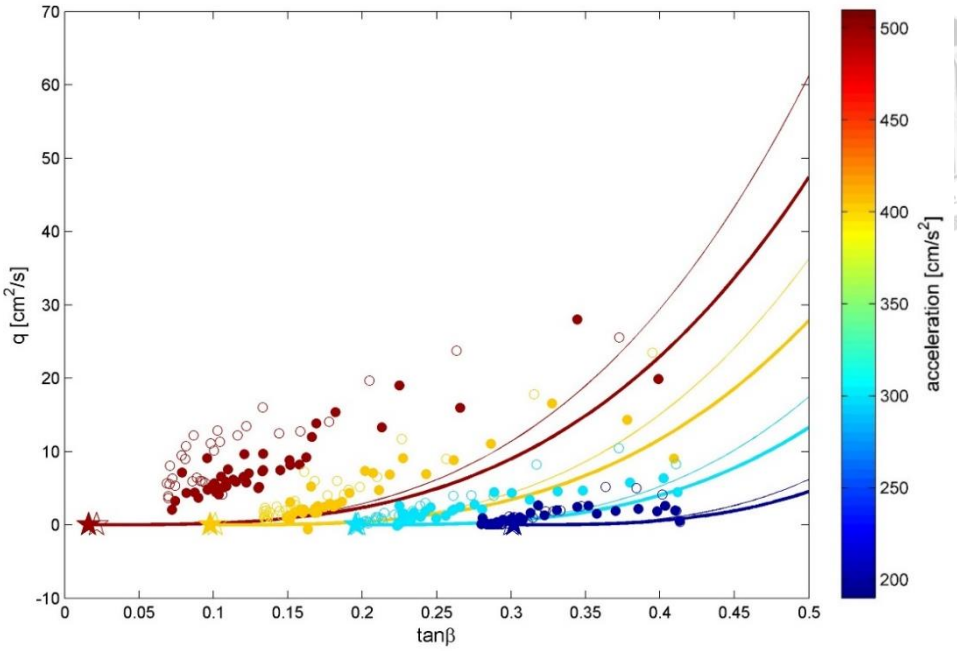

Fig. 4-17 The relation of $\tan\beta$ and flux with $\alpha = 28.03°$. The color lines are theoretical results, the points are experiment data, the bold lines are frequency $= 4Hz$, the thin lines are frequency $= 3Hz$, and the color represents different accelerations.

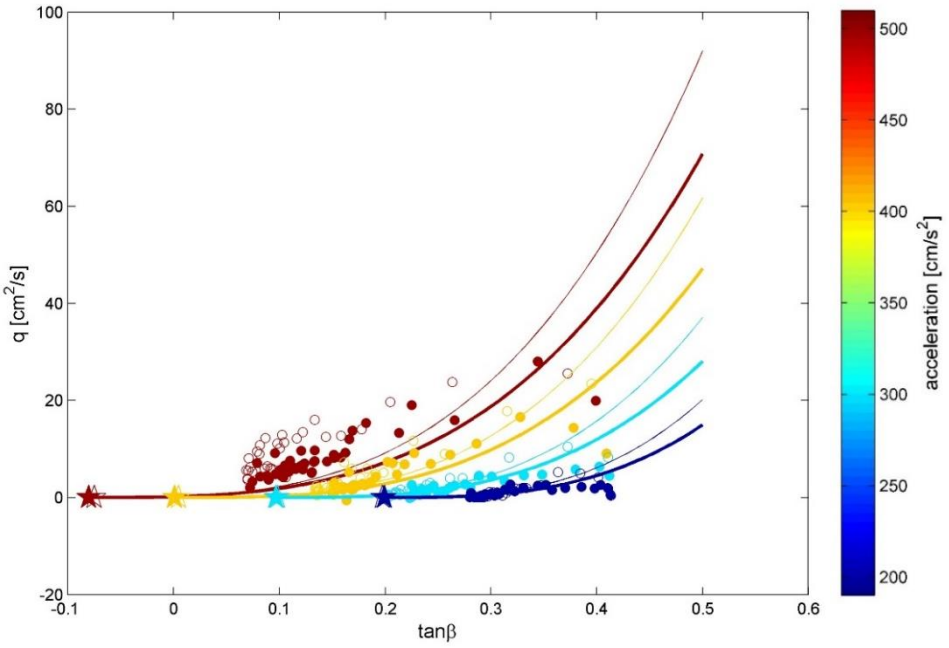

Fig. 4-18 The relation of $\tan\beta$ and flux with $\alpha = 22.5°$. The color lines are theoretical results, the points are experiment data, the bold lines are frequency $= 4Hz$, the thin lines are frequency $= 3Hz$, and the color represents different accelerations.

doi:10.6342/NTU201603286

Chapter 5 Conclusion

In this research, two numerical models which are derived from the governing equations and the depth-integrated equations are used to solve the granular flow problem, and the results of numerical solution and analytical solution are the same in the case of a dense granular flow over loose bed in a narrow channel. It means that both these two methods can be used to solve these flow problems. Furthermore, we use the numerical model to solve the problem of the granular flow under seismic conditions, and can obtain the velocity profile, flow depth, and flux under different initial conditions. Moreover, we can observe the situation that the direction of velocity will change as the vibration.

We conducted 12 rounds experiments with 3 different sizes observation regions. The initial condition of slope can be fixed with the frame, and the maximum acceleration can be defined by fitting the PTV data. Since the high speed camera is located on the ground, we remove the displacement of each photos and transform the coordinates system. The image results indicate that our method and process to adjust the photos is workable. Moreover, the PTV results also show that the image analysis method is applicability and the slope behavior is similar under the same conditions. This result supports our PTV method and repeatability of experiments.

With the results from PTV method, we can see the slope behavior and flow layer clearly. The PTV results also can provide the data to calculate the time-evolving variables, and we can observe the variation of flux, velocity profile, maximum velocity, surface shape and slope with time. When focus on the sections within a period, we can observe the periodic variation.

We derive the relation of slope and flux from our numerical model and experimental data fitting. Then, we plot the results together and can observe that the trend is similar

doi:10.6342/NTU201603286

between theoretical and experimental analysis.

doi:10.6342/NTU201603286

REFERENCES

Capart, H., Young, D. L., & Zech, Y. (2002). "Voronoï imaging methods for the measurement of granular flows." Experiments in Fluids, 32(1), 121-135.

Capart, H., Hung, C. Y., & Stark, C. P. (2015). "Depth-integrated equations for entraining granular flows in narrow channels." *Journal of Fluid Mechanics*, 765, R4.

Capart, H. (2016). BatchSeismicImplicitViscoplastic. Unpublished computer code, National Taiwan University.

Chou, H. T., Lee, C. F., & Chen, S. C. (2013). The Collapse Process of Granular Slopes Under Seismic Forcing. In *Earthquake-Induced Landslides* (pp. 45-57). Springer Berlin Heidelberg.

Jop, P., Forterre, Y., & Pouliquen, O. (2005). "Crucial role of sidewalls in granular surface flows: consequences for the rheology." Journal of Fluid Mechanics, 541, 167-192.

Lin, M. L., & Wang, K. L. (2006). "Seismic slope behavior in a large-scale shaking table model test." Engineering Geology, 86(2), 118-133.

Newmark, N.M., 1965. Effects of earthquake on dams and embankments. Géotechnique 15 (2), 139–160

Savage, S. B., & Hutter, K. (1991). "The dynamics of avalanches of granular materials from initiation to runout. Part I: Analysis." Acta Mechanica, 86(1-4), 201-223.

doi:10.6342/NTU201603286